Research Paper

Detoxifying SARS-CoV-2 antiviral drugs from model and real wastewaters by industrial waste-derived multiphase photocatalysts

Mirabbos Hojamberdiev [a,*], Bożena Czech [b,*], Anna Wasilewska [b], Anna Boguszewska-Czubara [c], Kunio Yubuta [d], Hajime Wagata [e], Shahlo S. Daminova [f,g], Zukhra C. Kadirova [f,g], Ronald Vargas [h]

[a] *Institut für Chemie, Technische Universität Berlin, Straße des 17. Juni 135, 10623 Berlin, Germany*
[b] *Department of Radiochemistry and Environmental Chemistry, Institute of Chemical Sciences, Faculty of Chemistry, Maria Curie-Skłodowska University, Pl. M. Curie-Skłodowskiej 3, 20-031 Lublin, Poland*
[c] *Department of Medical Chemistry, Medical University of Lublin, Chodźki 4a, Lublin 20-093, Poland*
[d] *Department of Applied Quantum Physics and Nuclear Engineering, Kyushu University, Fukuoka 819-0395, Japan*
[e] *Department of Applied Chemistry, School of Science and Technology, Meiji University, Kawasaki 214-8571, Japan*
[f] *Department of Inorganic Chemistry, National University of Uzbekistan, Tashkent 100174, Uzbekistan*
[g] *Uzbekistan-Japan Innovation Center of Youth, University Str. 2B, Tashkent 100095, Uzbekistan*
[h] *Instituto Tecnológico de Chascomús (INTECH) - Consejo Nacional de Investigaciones Científicas y Técnicas (CONICET) / Universidad Nacional de San Martín (UNSAM), Avenida Intendente Marino, Km 8,2, B7130IWA Chascomús, Provincia de Buenos Aires, Argentina*

HIGHLIGHTS

- Low-cost multiphase photocatalysts are synthesized from industrial waste and WO_3.
- Effects of calcination temperature and WO_3 concentration are investigated.
- Photocatalysts favor the photocatalytic oxidation of lopinavir and ritonavir.
- Ritonavir is removed with 95% efficiency after visible light irradiation for 15 min.
- No toxicity is detected using *Danio rerio* for treated ritonavir-containing wastewater.

GRAPHICAL ABSTRACT
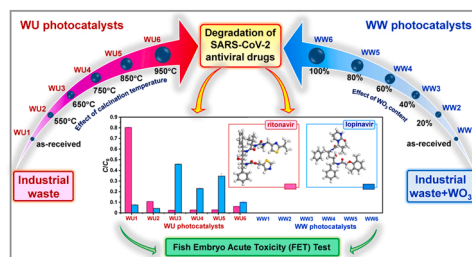
ABSTRACT

The use of antiviral drugs has surged as a result of the COVID-19 pandemic, resulting in higher concentrations of these pharmaceuticals in wastewater. The degradation efficiency of antiviral drugs in wastewater treatment plants has been reported to be too low due to their hydrophilic nature, and an additional procedure is usually necessary to degrade them completely. Photocatalysis is regarded as one of the most effective processes to degrade antiviral drugs. The present study aims at synthesizing multiphase photocatalysts by a simple calcination of industrial waste from ammonium molybdate production (*WU* photocatalysts) and its combination with WO_3 (*WW* photocatalysts). The X-ray diffraction (XRD) results confirm that the presence of multiple crystalline phases in the synthesized photocatalysts. UV–Vis diffuse reflectance spectra reveal that the synthesized multiphase photocatalysts absorb visible light up to 620 nm. Effects of calcination temperature of industrial waste (550–950 °C) and WO_3 content (0–100%) on photocatalytic activity of multiphase photocatalysts (*WU* and *WW*)

for efficient removal of SARS-CoV-2 antiviral drugs (lopinavir and ritonavir) in model and real wastewaters are studied. The highest k_1 value is observed for the photocatalytic removal of ritonavir from model wastewater using *WW4* (35.64 $\times 10^{-2}$ min^{-1}). The multiphase photocatalysts exhibit 95% efficiency in the photocatalytic removal of ritonavir within 15 of visible light irradiation. In contrast, 60 min of visible light irradiation is necessary to achieve 95% efficiency in the photocatalytic removal of lopinavir. The ecotoxicity test using zebrafish (*Danio rerio*) embryos shows no toxicity for photocatalytically treated ritonavir-containing wastewater, and the contrary trend is observed for photocatalytically treated lopinavir-containing wastewater. The synthesized multiphase photocatalysts can be tested and applied for efficient degradation of other SARS-CoV-2 antiviral drugs in wastewater in the future.

1. Introduction

In recent years, epidemic and pandemic viral diseases, such as swine influenza virus (H1N1), Ebola virus disease (EVD), Middle East respiratory syndrome coronavirus (MERS-CoV), severe acute respiratory syndrome coronavirus (SARS-CoV) and others have led to a significant increase in the usage of various antiviral drugs to treat viral infections. Consequently, water pollution with antiviral drugs, as an emerging class of anthropogenic pollutants, has become a global issue that poses a risk to human health and the aquatic environment (Thi et al., 2021) and triggers the development of various antiviral-resistant strains (Jain et al., 2013). An ongoing global pandemic of severe acute respiratory syndrome coronavirus 2 (SARS-CoV-2) has further increased an unprecedented use of antiviral drugs, accelerating the water pollution with various antiviral drugs (Choudhary et al., 2021). The degradation efficiency of those antiviral drugs in the wastewater treatment plants was reported to be too low due to their hydrophilic nature (Kosma et al., 2019), and an additional process is usually required to remove them completely. Therefore, advanced oxidation processes (AOPs) are a favorable alternative for the degradation and mineralization of antiviral drugs with high efficiency.

Heterogeneous photocatalysis is one of the sustainable advanced oxidation processes for efficient removal of various organic, inorganic, and microbial contaminants, where the formed reactive species with high oxidation power (e.g., $^\bullet$OH, $O_2^{\bullet-}$, h^+, $HO_2^\bullet$, etc.) are actively involved (Ibhadon and Fitzpatrick, 2013). Using commercial TiO$_2$-P25, 1-amantadine, 2-amantadine, and rimantadine were removed with the mineralization efficiencies of 88.7%, 90.8%, and 91.7%, respectively, under UV light irradiation, where the role of $^\bullet$OH species was significantly dominant over the photogenerated holes (An et al., 2015a). Similarly, the contribution of $^\bullet$OH species was substantial compared to the photogenerated holes in the degradation of Tamiflu (oseltamivir phosphate) via forming the typical intermediate species, such as hydration derivatives, hydroxyl substitutes and keto-derivatives (Wang et al., 2015), and in the degradation of acyclovir via hydroxylation, cleavage of isocytosine moieties, and H abstraction (An et al., 2015b) by TiO$_2$-P25. The degradation of zanamivir by TiO$_2$-P25 using a light source with lower irradiance (495 W•m^{-2}) was accelerated by a factor of 20, whereas a comparable result was obtained with higher irradiance (2700 W•m^{-2}), indicating the limitation by oxygen diffusion (Woche et al., 2016). Since the UV light makes up a small portion of the solar spectrum and is barely present in indoor premises, it is necessary to involve visible-light-active photocatalysts for the efficient removal of various antiviral drugs. Recently, Z-scheme Bi/BiVO$_4$-CdS heterojunction (Xue et al., 2021) and CdS-decorated BiVO$_4$ (Wu et al., 2020) have exhibited superior performance for the photocatalytic degradation of tetracycline hydrochloride under visible light irradiation, which was also found to have a beneficial effect in preventing the viral infection of SARS-CoV-2 from progressing if it is used in the early stage (Mosquera-Sulbaran and Hernández-Fonseca, 2021). Conversely, even though acyclovir was efficiently degraded using the g-C$_3$N$_4$/TiO$_2$ hybrid photocatalyst under visible light irradiation, three persistent intermediates were formed via (i) the mono-hydroxylation of the purine ring and the breakdown of the C–C bond from the side chain of acyclovir (P1), (ii)

the breakdown of the purine ring in acyclovir (P2), and (iii) the loss of the side chain from acyclovir (P3), which resisted a complete mineralization, and the aquatic toxicity of the third intermediate (P3) was also two times higher than that of acyclovir (Li et al., 2016). Therefore, it is necessary to conduct ecotoxicity tests for the photocatalytically treated water samples to demonstrate the efficiencies of the photocatalyst and photodegradation process.

Recently, inexpensive, environmentally friendly, and high-value-added materials derived from various wastes have shown efficient photocatalytic and sensing performance (Rodríguez-Padrón et al., 2020; Hojamberdiev et al., 2020a). For instance, the ZnS-containing waste from the mining-metallurgy industry was used as a starting material for the synthesis of trigonal ZnIn$_2$S$_4$ layered crystals by a binary-flux method, which exhibited a photocatalytic H$_2$ evolution rate of 232 μmol•h^{-1} (Hojamberdiev et al., 2018). The ZnS-containing waste was also combined with SnO$_2$ (Hojamberdiev et al., 2020b) and ZnO (Vargas et al., 2022) for the efficient photocatalytic degradation of metoprolol (beta-blocker), carbamazepine (antiepileptic), acetaminophen (nonsteroidal anti-inflammatory drug), and triclosan (antimicrobial) in model wastewater and photoelectrochemical water oxidation, respectively. Also, the antibacterial activity of the ZnS-containing waste was evaluated against four bacterial strains, and the highest antibacterial activity was observed for the inactivation of *E. coli* (99%) within 2 h of UV light irradiation (Hojamberdiev et al., 2019).

Tungsten oxide (WO$_3$) is an *n*-type semiconductor that can absorb visible light up to 480 nm and has good photostability, electron-transport property, and sufficient valence-band potential to drive oxidation reaction (Quan et al., 2020). Previously, we have succeeded in enhancing the photocatalytic activity of the ZnS-containing waste for the degradation of metoprolol, triclosan, and caffeine both in individual and mixed solutions under visible light irradiation by involving hexagonal WO$_3$ and WO$_3$•0.5 H$_2$O (Czech et al., 2020). In this work, we report on the synthesis of inexpensive multiphase photocatalysts by a simple calcination of industrial waste from ammonium molybdate production (*WU* photocatalysts) and its combination with WO$_3$ (*WW* photocatalysts). The effects of calcination temperature of industrial waste (550–950 °C) and WO$_3$ content (0–100%) on photocatalytic activity of multiphase photocatalysts (*WU* and *WW*) for efficient removal of SARS-CoV-2 antiviral drugs (lopinavir and ritonavir) in model and real wastewaters are studied. The kinetics and mechanisms of the photodegradation of lopinavir and ritonavir by the synthesized multiphase photocatalysts are explored. Further, to analyze the ecotoxicity of the photocatalytically treated water and wastewater samples, the Fish Embryo Acute Toxicity (FET) test is conducted using zebrafish (*Danio rerio*) embryos according to the OECD Guidelines.

2. Experimental

2.1. Synthesis of multiphase photocatalysts

The *WU* photocatalysts were prepared by calcination of industrial waste, generated during the production of ammonium molybdate (Almalyk Mining-Metallurgical Complex, Uzbekistan), at temperatures ranging from 550 °C to 950 °C for 2 h. The *WU* photocatalysts were

denoted as *WU1* (as-received), *WU2* (550 °C), *WU3* (650 °C), *WU4* (750 °C), *WU5* (850 °C), and *WU6* (950 °C) with respect to their calcination temperature. The *WW* photocatalysts were prepared by mixing the calcined industrial waste at 850 °C for 5 h and WO_3 (99.9%, Merck) in different ratios and calcination at 850 °C for 2 h. The *WW* photocatalysts were labeled as *WW1* (10:0), *WW2* (8:2), *WW3* (6:4), *WW4* (4:6), *WW5* (2:8), and *WW6* (0:10) according to the calcined industrial waste:WO_3 ratio.

2.2. Characterization of multiphase photocatalysts

The X-ray diffraction (XRD) patterns were recorded on a MiniflexII (Rigaku) diffractometer to identify the crystalline phases in the synthesized multiphase photocatalysts. The micro- and nanostructures of multiphase photocatalysts were examined by using an S-5200 field-emission-type scanning electron microscope (Hitachi) and an EM-002B high-resolution transmission electron microscope (TOPCON), respectively. The ultraviolet-visible (UV–Vis) diffuse reflectance spectra of multiphase photocatalysts were measured on a UV-3600 UV–Vis–NIR spectrophotometer (Shimadzu). The surface chemical states were analyzed by X-ray photoelectron spectroscopy (JPS-9000SX, JEOL) with non-monochromated Mg-K$_\alpha$ radiation (1253.6 eV). The surface charge density was estimated using the data obtained by potentiometric titration using 0.001 mol•dm^{-3} NaNO$_3$ as the background electrolyte (Broda et al., 2021).

Metrohm-DropSens (DS110) screen-printed carbon electrodes were used, and all potentials were referenced to the Ag-AgCl reference electrode. The carbon surface of the screen-printed electrodes was modified using only *WU6* and *WW6* photocatalysts by applying the dip-coating protocol. The suspension was prepared by dispersing 1.0 mg of *WU6* or *WW6* in 0.5 mL of a mixture solution of ethanol and water (1:1 ratio) under ultrasonication for 10 min, deposited on the electrodes (15 μL suspension), and dried using a heating gun for 10 min. The deposited photocatalyst powders were estimated to be ~0.2 mg•cm^{-2} for both electrodes. The irradiated geometric area of the photoanodes was 0.13 cm^2, and the electrolyte volume was 50 μL. The photoelectrochemical measurements were conducted in 0.1 M Na$_2$SO$_3$ (or Na$_2$SO$_4$) N$_2$-saturated solution using a Potentiostat/Galvanostat (DropSens μSTAT200). LED solar light with the irradiance of ~100 mW•cm^{-2} (Solar Light, G2V) was used. The scan rate for linear sweep voltammetry (LSV) was 2 mV•s^{-1}, and the chronoamperometric (CA) analysis at 0.6 V and 1.2 V vs. Ag-AgCl was performed using a chopped light mode (light-dark cycle: 60–60 s). The stability test was carried out by CA measurement at 1.2 V vs. Ag-AgCl for 60 min under continuous irradiation and in the dark.

The details of photocatalytic tests for the removal of SARS-CoV-2 antiviral drugs (lopinavir and ritonavir) from contaminated model and real wastewaters (A.2.1.) and the Fish Embryo Acute Toxicity (FET) test of photocatalytically treated model and real wastewater samples (A.2.2.) are given in Supplementary Material.

3. Results and discussion

3.1. Characterization of multiphase photocatalysts

The XPS survey spectra of *WU6* and *WW6* photocatalysts are shown in Fig. A.1a and A.1b, respectively. As shown, the *WU6* comprises of iron, molybdenum, magnesium, silicon, aluminum, calcium, oxygen, and adventitious carbon, whereas the *WW6* consists of tungsten, oxygen, and adventitious carbon. In Fig. 1, the reflections in the XRD pattern of the as-received industrial waste (*WU1*) are broad possibly due to overlapping and the presence of amorphous phases. In the *WU1*, molybdenum exists in the forms of various molybdates, along with calcium, magnesium, iron, etc., with different oxidation states and ordered molybdate intercalates of hydrotalcite-like compounds $(3[Mg_6Al_2(OH)_{16}][Mo_7O_{24}]•48H_2O)$ (Hibino and Tsunashima, 1997). Due to a low concentration of other

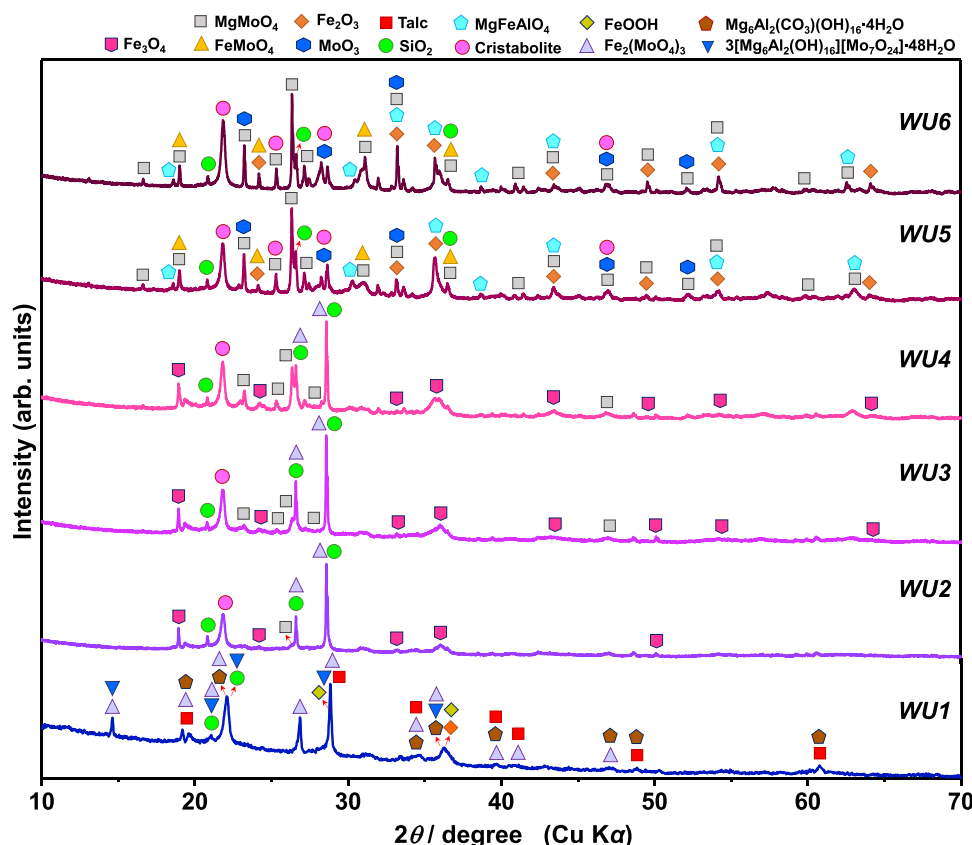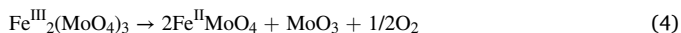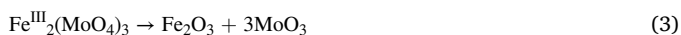**Fig. 1.** XRD patterns of *WU* photocatalysts.

elements, iron with a higher concentration is present in the form of $Fe_2(MoO_4)_3$ (Tian et al., 2011). Thus, the high concentration of iron (FeOOH and Fe_2O_3) leads to the formation of mixed-valence compounds $[Fe^{III}Mo^{VI}O^{2-}_4]_X = [Fe^{III}(Mo^{VI}O^{2-}_4)_{X-1}(Mo^VO^{3-}_4)]$ and ammonium molybdoferrate $(NH_4)_3H_6[Fe^{III}(Mo^{VI}O_4)_6]$ (Nikolenko et al., 2018). Additionally, the reflections of some natural minerals, including quartz (SiO_2), talc $(Mg_3Si_4O_{10}(OH)_2)$, and hydrotalcite $(Mg_6Al_2(CO_3)(OH)_{16} \cdot 4H_2O)$, are also observed. After calcination of the as-received industrial waste in the temperature range from 550 °C to 750 °C (*WU2-WU4*), Fe_3O_4, SiO_2, $Fe_2(MoO_4)_3$, $MgMoO_4$, and β-cristobalite become predominant crystalline phases. In this temperature range, the thermal decomposition of hydrotalcites to their corresponding oxides, such as MgO, MoO_3, and $MgFeAlO_4$, proceeds along with the simultaneous dehydroxylation and decarbonation of the hydrotalcite structure (Palmer et al., 2009). The high-temperature reaction between MgO and MoO_3 results in the formation of $MgMoO_4$ (Yoon et al., 1999).

$$2MgO + Fe_2O_3 + Al_2O_3 \rightarrow 2MgFeAlO_4 \tag{1}$$

$$MgO + MoO_3 \rightarrow MgMoO_4 \tag{2}$$

A further increase in the calcination temperature of the as-received industrial waste up to 950 °C (*WU5-WU6*) causes a partial decomposition of $Fe_2(MoO_4)_3$ to Fe_2O_3 and MoO_3 and the formation of $FeMoO_4$.

$$Fe^{III}_2(MoO_4)_3 \rightarrow Fe_2O_3 + 3MoO_3 \tag{3}$$

$$Fe^{III}_2(MoO_4)_3 \rightarrow 2Fe^{II}MoO_4 + MoO_3 + 1/2O_2 \tag{4}$$

Also, SiO_2 and β-cristobalite were formed at high temperatures (Parise et al., 1994). Due to its low concentration in the as-received industrial waste, the crystalline phases containing calcium are not observed in the XRD patterns of the *WU* photocatalysts.

In Fig. 2, the industrial waste calcined at 850 °C for 5 h (*WW1*) consists of $MgMoO_4$, $FeMoO_4$, SiO_2, cristobalite, MoO_3, Fe_2O_3, and

$MgFeAlO_4$. When the industrial waste:WO_3 ratio is set to 8:2 (*WW2*), the reflections assignable to $MgWO_4$ appear as the reaction product of MgO and WO_3, whereas the reflections of $MgFeAlO_4$ disappear completely.

$$MgO + WO_3 \rightarrow MgWO_4 \tag{5}$$

When the industrial waste:WO_3 ratio is adjusted to 6:4 (*WW3*), the reflections of MoO_3, $MgMoO_4$, and $FeMoO_4$ disappear completely, whereas the reflections of $FeWO_4$ and $Fe_{0.184}Mg_{1.816}SiO_4$ appear. In the industrial waste:WO_3 ratios of 4:6 (*WW4*) and 2:8 (*WW5*), Fe_2O_3 and $Fe_{0.184}Mg_{1.816}SiO_4$ disappear, and SiO_2 is fully converted to β-cristobalite (Parise et al., 1994), whereas $FeWO_4$ (Sieber et al., 1982) along with $MgWO_4$ and $Fe_2Mo_3O_{12}$ become dominant crystalline phases.

$$1/3Fe_2O_3 + 1/3Fe + WO_3 \rightarrow 2FeWO_4 \tag{6}$$

$$FeO + WO_3 \rightarrow FeWO_4 \tag{7}$$

$$Fe_2O_3 + 3MoO_3 \rightarrow Fe_2Mo_3O_{12} \tag{8}$$

As expected, in the industrial waste: WO_3 ratio of 0:10, hexagonal WO_3 is the only crystalline phase. The XRD results show that Fe_3O_4 (2% in *WU2*, 3% in *WU3*, 9% in *WU4*, and 3% in *WU5*), Fe_2O_3 (26% in *WU2*, 6% in *WU5*, and 13% in *WU6*), $MgMoO_4$ (41% in *WU2* and 23% in *WU3*), $FeMoO_4$ (17% in *WU5* and 30% in *WU6*), and $MgFeAlO_4$ (37% in *WU5* and 7% in *WU6*), MoO_3 (11% in *WU5* and 16% in *WU6*), crystalline phases are dominant in the *WU* photocatalysts, whereas Fe_2O_3 (5% in *WW2*, 6% in *WW4*, and 14% in *WW5*), $FeWO_4$ (3% in *WW2*, 17% in *WU3*, 26% in *WW4*, and 30% in *WW5*), $MgWO_4$ (36% in *WW2*, 58% in *WU3*, 50% in *WW4*, and 47% in *WW5*), and $Fe_2Mo_3O_{12}$ (17% in *WW2*, 10% in *WU3*, 8% in *WW4*, and 11% in *WW5*) crystalline phases are prevalent in the *WW* photocatalysts. Identifying the crystalline phases present in both *WU* and *WW* photocatalysts allows us to understand the photodegradation mechanism of SARS-CoV-2 antiviral drugs (lopinavir and ritonavir) by industrial waste-derived multiphase photocatalysts.

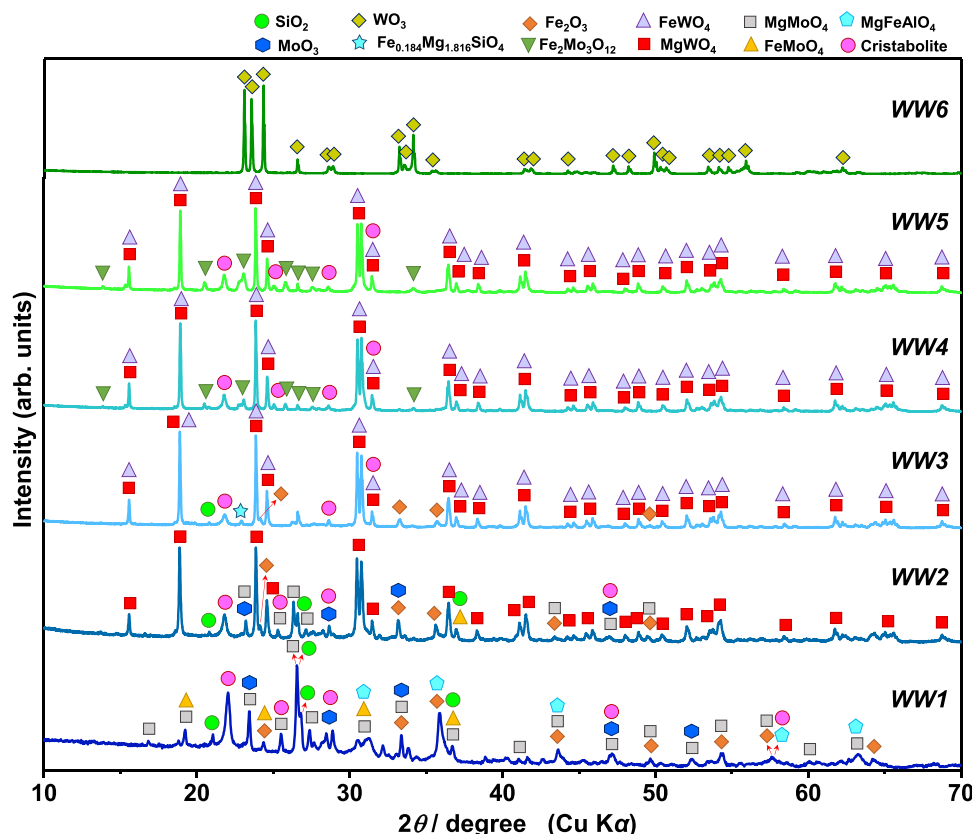The SEM images of selected *WU* and *WW* photocatalysts are shown in

Fig. 2. XRD patterns of *WW* photocatalysts.

Fig. 3. The *WU1* shows an irregular morphology composed of nanoparticles (Fig. 3a). In contrast, submicron-sized rods are formed on the surface of irregular particles (Fig. 3b) after the calcination of the as-received industrial waste at 950 °C (*WU6*). These submicron-sized rods possibly belong to one of the crystalline phases formed at 950 °C. Similarly, the *WW1* possesses particles of different sizes and morphologies (Fig. 3c). At the industrial waste:WO$_3$ ratio of 4:6 (*WW4*), the submicron-sized particles belonging to either FeWO$_4$/MgWO$_4$ or Fe$_2$Mo$_3$O$_{12}$ are formed on the surface (Fig. 3d). The *WW6* contains micron-sized cuboids and double-cuboids, formed by the assembly of small and large idiomorphic crystals, along with irregular particles (Fig. 3e). In Fig. A.2a, the TEM image shows that the *WU6* has quasi-spherical particles with a size of < 200 nm along with rod-like microstructures. The TEM image shown in Fig. A.2b reveals the flake-like morphology consisted of nanoparticles. The HRTEM image and SAED patterns confirm the presence of multiple phases with polycrystalline nature in the *WU6* and *WW4* photocatalysts. The TEM image in Fig. A.2c shows the WO$_3$ crystals with idiomorphic shape, and the HRTEM image and SAED pattern confirm the high crystallinity and single-crystalline nature of the WO$_3$ crystals, respectively.

The UV–Vis diffuse reflectance spectra of the *WU* and *WW* photocatalysts are shown in Fig. 4a and b, respectively. In Fig. 4a, the *WU1* shows an absorption edge at about 620 nm, which shifts toward lower wavelengths (600 nm) for the *WU2* and *WU3* after calcination at 550 °C and 650 °C, respectively. A further increase in the calcination temperature to 750 °C, 850 °C, and 950 °C similarly leads to a slight redshift in the absorption edge (610 nm) for the *WU4*, *WU5*, and *WU6* photocatalysts, respectively. This suggests that the *WU* photocatalysts can absorb visible light due to the presence of visible-light-active crystalline phases, such as Fe$_2$O$_3$, Fe$_3$O$_4$, FeMoO$_4$, and MgFeAlO$_4$. The powder color of the *WU* photocatalysts changes from dark reddish-brown to dark brown with the increase in the calcination temperature up to 950 °C. In the *WW* photocatalysts (Fig. 4b), the *WW1* and *WW2* exhibit similar absorption edges at about 610 nm. A further increase in the industrial waste:WO$_3$ ratio leads to a slight blueshift (about 600 nm) in the absorption edges of the *WW3*, *WW4*, and *WW5*. The *WW1-WW5* photocatalysts can absorb more photons from visible light compared with the *WW6* because of the existence of visible-light-active crystalline phases, such as Fe$_2$O$_3$, FeWO$_4$, and Fe$_2$Mo$_3$O$_{12}$. The *WW6*, which contains only WO$_3$, shows an absorption edge at 470 nm, which corresponds to the bandgap energy of 2.64 eV. The powder color of the *WW1-WW5* photocatalysts changes from reddish-brown to pale brown with the increase in the industrial waste:WO$_3$ ratio, and the *WW6* has a light-yellow color.

3.2. Photoelectrochemical characterization

The photoelectrochemical response of the *WU6* and *WW6*, as the representatives of *WU* and *WW* photocatalysts, was evaluated using linear scan voltammetry (LSV). Fig. 5a shows the photoelectrochemical response of the *WW6* and *WU6* photoanodes under continuous light conditions and in the dark. Particularly, the effect of the presence and absence of SO$_3^{2-}$ as a hole scavenger in the aqueous solution was determined. When irradiated, a significant increase in the anodic response as a function of potential was observed, followed by a change in the slope until a pseudo-stationary state in the photocurrent signal was defined at high overpotentials (Bedoya-Lora et al., 2021; Peter, 2018). This is a typical increase caused by the arrival of new minority charge carriers at the semiconductor-electrolyte interface, where holes participate in the chemical reactions with the donor species in the solution (in this case, SO$_3^{2-}$ and H$_2$O) (Ng et al., 2012; Zhang et al., 2014). Very low photocurrent intensities were observed in the absence of SO$_3^{2-}$, which increased at higher potentials, showing kinetic limitations due to the importance of charge carrier recombination processes (Peter, 2018; Zhang et al., 2014). The respective onset potentials (vs. Ag-AgCl) of the *WW6* and *WU6* photoanodes are 0.41 V and 0.28 V in the presence of SO$_3^{2-}$ and 0.50 V and 0.48 V in the absence of SO$_3^{2-}$, respectively. This is

consistent with previous reports on WO$_3$-based electrodes (Ng et al., 2012; Gomis-Berenguer et al., 2018; Patil and Patil, 1996; Costa et al., 2020; Núñez et al., 2019).

Fig. 5b shows the chronoamperometric response at high overpotential (1.2 V vs. Ag-AgCl) for 60 min to confirm the stability of the fabricated *WU6* and *WW6* electrodes. As shown, a stationary photocurrent density magnitude in a time interval is greater than that of the experimental measurements: 0.17 mA•cm^{-2} for *WW6* and 0.12 mA•cm^{-2} for *WU6*. It is important to compare the photocurrent signals obtained for *WW6* and *WU6* to understand the effect of different chemical natures of the fabricated photoanodes on their photoelectrochemical response. Fig. 5a shows the photocurrent density vs. potential plot, indicating that the photoanodes differ in the following ways: (i) at high overpotentials, the photocurrent of the *WW6* is higher, (ii) the photocurrent signal of the *WU6* begins at more negative potentials than that of the *WW6*, and (iii) at low overpotentials, the *WU6* defines higher photocurrent values than the *WW6*. Changes in material synthesis, chemical composition, crystallinity, particle size, and other factors modified the balance between charge transfer and recombination kinetics differently in the *WU6* and *WW6* (Patil and Patil, 1996; Hojamberdiev et al., 2021). To elucidate the differences in the photo-redox processes between the *WW6* and *WU6*, it is essential to analyze the photoelectrochemical properties in the presence of SO$_3^{2-}$ in the aqueous solution since a higher photocurrent is guaranteed by its reaction with holes (Zhang et al., 2014). The effect of the photon flux is evident in the modulated illumination condition at different potentials, as shown in the chronoamperometry (CA) results in Fig. 5c and 5d. Because the charge carriers are rapidly deactivated by recombination when the incident photon flux is interrupted, the photocurrent in both electrodes decreases to the values obtained in the dark. The separation of the electron-hole pair occurs quickly as the photonoade surface is re-illuminated, resulting in the concentration of these carriers reaching the level required to maintain the photocurrent observed under continuous illumination (Patil and Patil, 1996; Hojamberdiev et al., 2021).

It should also be highlighted that (i) after the initial seconds of irradiation, an anodic photocurrent peak (overshoot) is detected at low overpotential (0.6 V vs. Ag-AgCl). Undershoots were detected when the light was turned off, as expected for photocatalysts that exhibit surface recombination events. These characteristics are related to the differences in electron and hole relaxation time (Patil and Patil, 1996; Peter et al., 2020). (ii) In both light and dark conditions, stable photocurrents were promptly generated at high overpotential (1.2 V vs. Ag-AgCl), and (iii) the quasi-stationary photocurrent increased with applied potential, indicating the inverse effect between charge transfer and bulk recombination processes (Peter, 2018; Patil and Patil, 1996; Peter et al., 2020). This is consistent with the data reported previously for the WO$_3$/nanoporous carbon composite (Gomis-Berenguer et al., 2018), Fe$_2$O$_3$ (Li et al., 2021), and Fe$_2$O$_3$/WO$_3$ (Muller et al., 2017) photoanodes.

In general, the chemical and structural modifications made by the synthesis method influence the optoelectronic properties, which manifest as a variation in the photoelectrochemical response (Hojamberdiev et al., 2021; Monllor-Satoca et al., 2020). Under light conditions and applied potential, electrons are drawn into the external circuit, but they can also be trapped in new mid-gap states introduced by defects, heterojunctions, and other factors (Monllor-Satoca et al., 2020; Low et al., 2017). The photoelectrochemical response of the *WW6* and *WU6* photoanodes is then specified by (i) the imposed energy condition and (ii) the specific property of semiconductors. While the former can be modulated by changing the applied potential, the latter can be evidenced by modifying the photocatalyst structure. When these types of modifications are made, the mid-gap states of the semiconductors and the kinetics of the processes that occur in the spatial charge zone (SCZ) are frequently affected (Monllor-Satoca et al., 2020). The lifetimes of charge carriers in the WO$_3$ photoanode have been found to range from ultra-fast timescales up to the order of seconds, depending on the kinetic
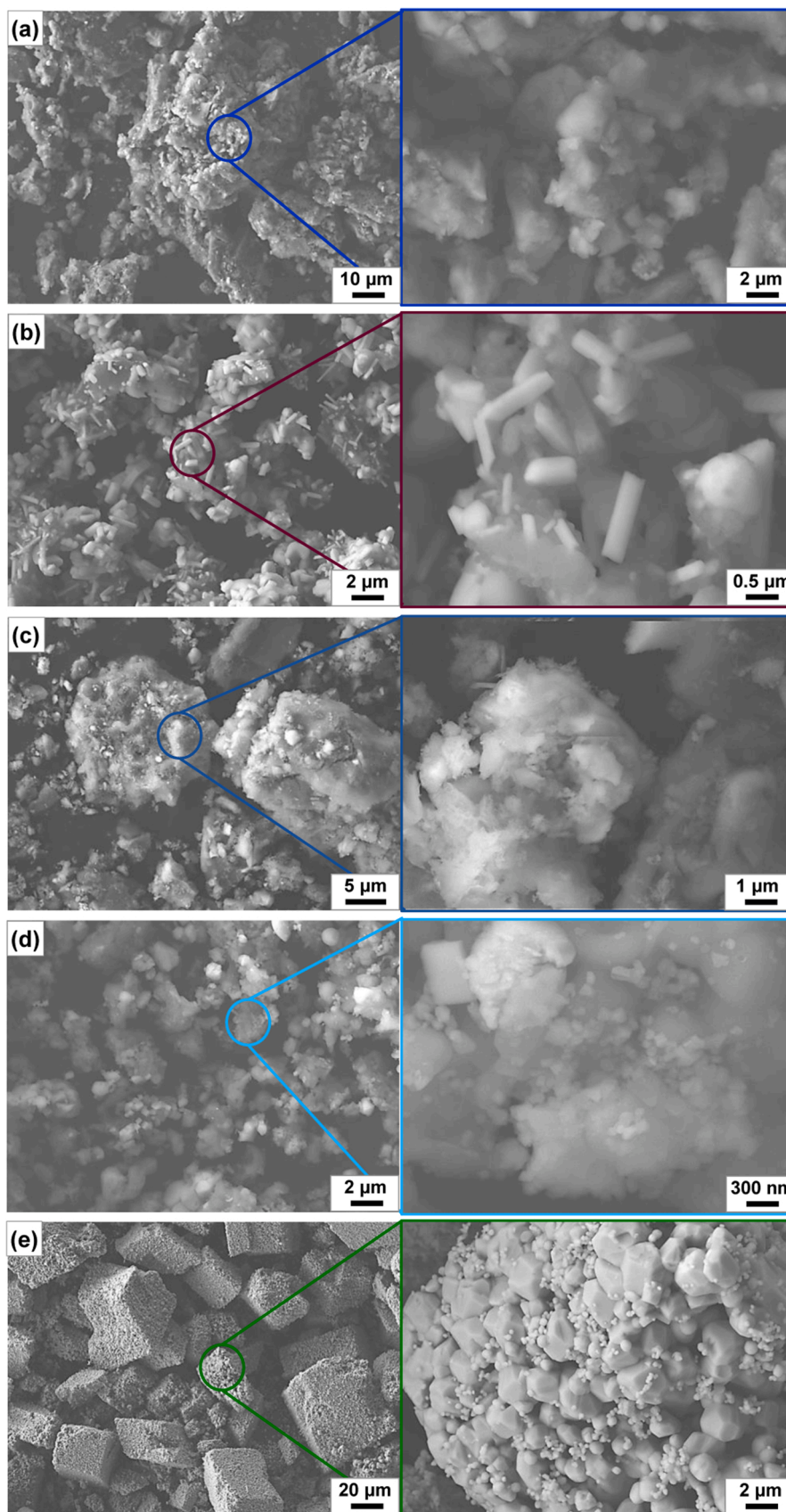
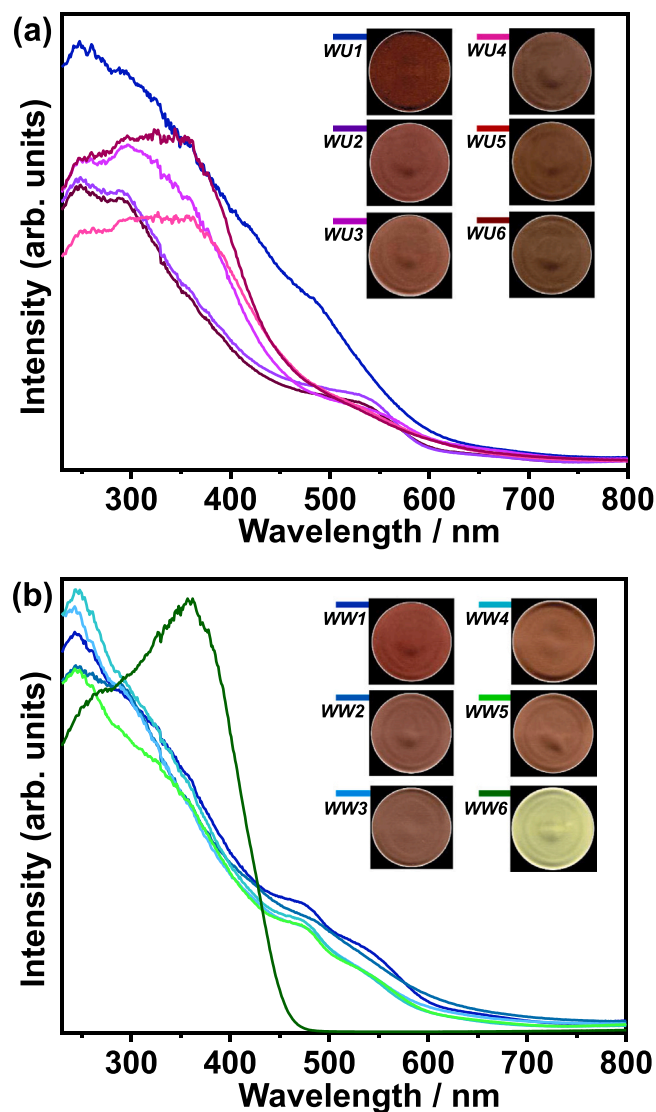**Fig. 3.** SEM images *WU1* (a), *WU6* (b), *WW1* (c), *WW4* (d), and *WW6* (e) photocatalysts.

Fig. 4. UV–Vis diffuse reflectance spectra of *WU* (a) and *WW* (b) photocatalysts.

process in the SCZ (Corby et al., 2019). The photoelectrochemical results show that modifying the synthesis parameters and chemical and phase compositions of *WW6* and *WU6* can modulate the electronic properties that govern carrier deactivation processes. As a result, it is expected that the combinations of *WW6* and *WU6* can have an enhanced photocatalytic activity. It should be noted that (i) at low overpotential, the *WU6* has less recombination than the *WW6*, and (ii) at high overpotential, the *WW6* is more likely to promote photo-redox processes than the *WU6*. Changes in the kinetics of the processes that allow charge carriers to react with chemical species in the electrolyte occur in all cases. Due to dramatic alterations in the recombination kinetics of charge carriers, the modifications made for the *WU* and *WW* photocatalysts promote more effective photocatalytic processes. Because of a decrease in the recombination rate, the electrochemical assistance of photocatalysis is expected to favor the efficiency of charge transfer in the *WW* and *WU* photocatalysts. In all cases, a trend in the improvement of the photocatalytic process in the presence of the synthesized multiphase photocatalysts is envisaged. Therefore, the photodegradation of SARS-CoV-2 antiviral drugs (ritonavir and lopinavir) by the synthesized multiphase photocatalysts is a key step.

3.3. Photocatalytic removal of SARS-CoV-2 antiviral drugs

3.3.1. Photocatalytic removal of ritonavir in model wastewater

As shown in Fig. 6a, the photolysis of ritonavir ($C_{37}H_{48}N_6O_5S_2$, 720.94 g•mol^{-1}, logK_{ow}=6.29) in model wastewater was very fast. After 15 min of visible light irradiation, ritonavir was completely degraded in model wastewater, indicating that ritonavir does not pose a significant risk to the environment. However, lopinavir and ritonavir should be removed with an efficiency of more than 80–90% (92% and 93%, respectively) based on the predicted environmental concentration (PEC) (Kuroda et al., 2021). However, the limited experimental data do not support this. Lopinavir and ritonavir removal rates were significantly lower in African WWTPs (43% to 71% for ritonavir and -192% to -58% for lopinavir), indicating their accumulation in the effluent (Abafe et al., 2018). Because lopinavir and ritonavir are widely used in HIV and COVID-19 treatment (Brown et al., 2021; Kou et al., 2021), their predicted environmental concentrations must be higher. Using quantitative structure-activity relationship modeling (considering 100 patients treated out of 100,000 populations a day), studies have predicted that currently used COVID-19 treatment drugs, including lopinavir and ritonavir, can be removed with a low removal efficiency (<20%) during traditional wastewater treatment, and their predicted environmental concentrations in the WWTP effluent can reach 730 ng•L^{-1} each (both unchanged forms and metabolites) (Kuroda et al., 2021). According to another study (Kumari and Kumar, 2021), the PECs of lopinavir and ritonavir in river water or fish might be 186 µg•L^{-1} and 239 µg•kg^{-1} and 128 µg•L^{-1} and 169 µg•kg^{-1}, respectively. In African WWTPs, the concentration of lopinavir was up to 2.5 µg• L^{-1} in influents and 3.8 µg•L^{-1} in effluents, and the concentration of ritonavir was up to 3.2 µg•L^{-1} (Abafe et al., 2018). Interestingly, some enrichment of lopinavir in the treated wastewater (tWW) was observed, highlighting the necessity of properly managing antiviral drug-contaminated wastewater. Due to the direct use of antiviral drug-containing wastewater in agriculture and animals, new strategies for treating antiviral drug-containing wastewater must be developed (Jain et al., 2013; Kuroda et al., 2021; Nannou et al., 2020).

The *WW* photocatalysts were effective in the photocatalytic treatment of model wastewater containing antiviral drugs. In the dark, the *WW6* (100% WO$_3$) exhibited the highest adsorption, with up to 65% ritonavir adsorbed. In the dark, the *WU* photocatalysts had a lower adsorption capacity for both antiviral drugs than the *WW* photocatalyst, with up to 15% ritonavir adsorbed (Fig. 6b). In previous work (Kovalova et al., 2013) on the adsorption of pharmaceuticals onto powdered activated carbon (at 25 mg•L^{-1}), more than 70% of ritonavir was adsorbed in less than 24 h. Except for the *WU1* (3[Mg$_6$Al$_2$(OH)$_{16}$]•[Mo$_7$O$_{24}$] •48 H$_2$O (9%), Fe$_2$(MoO$_4$)$_3$ (40%), and MgMoO$_4$ (<5%)), all *WU* photocatalysts showed high photocatalytic activity in the degradation of ritonavir. Surprisingly, the poor removal efficiency (up to 20% after 120 min of irradiation) remained steady, signifying the formation of certain persistent by-products. The chromatograms obtained with the *WU1* photocatalyst (detection at 254 nm) show only two additional peaks (R_t =1.1 min and R_t =1.9 min), but their relative areas were up to 30% of ritonavir and did not increase appreciably during the photocatalytic reaction (Fig. 6c).

The efficiency of the photocatalytic removal of ritonavir under visible light irradiation for 15 min was compared since the photocatalytic process was quite fast (Fig. 6d). When model wastewater was employed, the *WW* photocatalysts showed a reduced efficiency, with the lowest photocatalytic efficiency for the *WW2* (3% FeWO$_4$) and *WW5* (30% FeWO$_4$), despite the presence of FeWO$_4$. This implies that there are other factors in addition to the crystalline phases affecting the photocatalytic activity. Previously, direct Z-scheme nanocomposite coupling of the visible-light-active FeWO$_4$ nanoparticles with the C$_3$N$_4$ nanosheets exhibited excellent performance for CO production (Bhosale et al., 2019). The O 2p- and Fe 3d-like states hybridize in the valence-band region, whereas the empty Fe 4 s-like states are located at
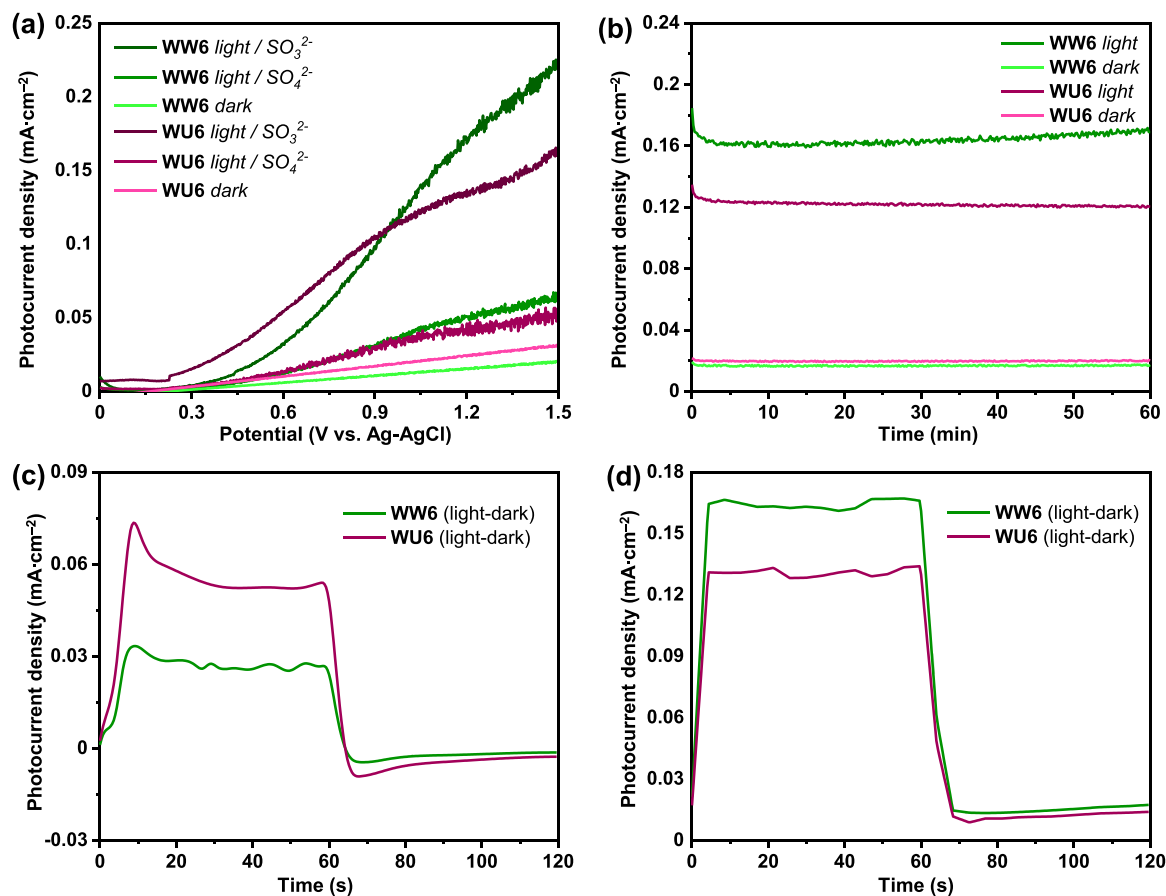
Fig. 5. Photoelectrochemical response of *WW6* and *WU6* photoanodes in 0.1 M Na$_2$SO$_3$ (or Na$_2$SO$_4$) N$_2$-saturated solution. Effects of simulated solar light and dark conditions: LSV at 2 mV•s⁻1 (a) and CA at 1.2 V vs. Ag-AgCl under continuous light and dark conditions (b). Light-dark cycles: CA at 0.6 V vs. Ag-AgCl (c) and CA at 1.2 V vs. Ag-AgCl (d).

the bottom of the conduction band and W 5d-like states are at the higher energy side of the conduction band of FeWO$_4$ (Rajagopal et al., 2010). In the photocatalytic process, iron, even in the form of FeWO$_4$, is expected to promote the formation of •OH radicals (Rajagopal et al., 2010; Li et al., 2019).

The *WU* photocatalysts showed the opposite trend. Despite the fact that direct photolysis of ritonavir was fast within 15 min of visible light irradiation, only photocatalytic treatment with *WU3* and *WU4* enabled a total removal of ritonavir from model wastewater. In comparison to the photocatalytic removal efficiency of nevirapine (an antiviral drug) over irradiated FL-BP@Nb$_2$O$_5$ (68% after 3 h of irradiation, pH = 3, m_{cat} = 15 mg, C_0 = 5 mg•L⁻¹) (Guo et al., 2013), the photocatalytic removal efficiency of ritonavir was substantially greater for the *WU3* and *WU4* photocatalysts. The presence of Fe$_3$O$_4$ (20%), Fe$_2$(MoO$_4$)$_3$ (17%), and MgMoO$_4$ (35%) phases in the *WU3* and *WU4* photocatalysts can explain the increased photocatalytic removal efficiency of ritonavir. Co-doping with Fe+Mo was also found to improve the photocatalytic activity of TiO$_2$ due to retarding the recombination process (Bhembe et al., 2020). The Fe^{3+} ions in the synthesized multiphase photocatalysts can increase absorption of visible light and mediate the charge-transfer process (Liu et al., 2012), whereas the Fe^{2+} ions can assist the heterogeneous photo-Fenton reactions (Kavitha and Palanivelu, 2004; Ruppert et al., 1993). In general, proposing a degradation pathway for lopinavir is challenging because it is thought to be stable under environmental conditions (Seshachalam et al., 2007; Donato et al., 2006). Despite this, lopinavir is susceptible to •OH attack due to the presence of different ketone, phenyl, and phenoxy groups (Kopinke and Georgi, 2017). The reaction rate constants with •OH radicals (considering molecules with

comparable structures or substructures to lopinavir and ritonavir) are estimated to be about 10⁹–10¹⁰ L mol⁻¹ s⁻¹) (Zwiener and Frimmel, 2000). Ritonavir is susceptible to hydrolytic cleavage because of the presence of carbamate and urea moieties (Tiwari and Bonde, 2011; Rao et al., 2010). The formation and decomposition of alkylperoxide radicals leading to the formation of relative alcohols, ketones, and carbon-chain fragmentation, which results in acyclic products, can be considered for the possible degradation pathway of ritonavir (Kopinke and Georgi, 2017).

The possible degradation pathway of ritonavir is shown in Fig. 7a. As shown, the hydrolysis of ritonavir may lead to the loss of 2-isopropyl-4-methylthiazole ion in the form of alcohol and the formation of C$_{30}$H$_{40}$N$_5$O$_5$S$^+$. Simultaneously, some extra isopropyl groups in the thiazole moiety of H$_2$O$_2$ might be formed on the surface of the synthesized multiphase photocatalysts due to the reaction of •OH with water molecules. Protonated amine may be formed by a further cleavage of the C–N bond, whereas alcohol is formed by hydrolysis of the carbamate bond (Miyazaki et al., 2017). Because of the hydrolysis and C–N bond cleavage, substituted acetamide and 2,6-dimethylphenoxy acetic acid are possibly produced as the oxidation products of lopinavir (Fig. 7b) (Chitturi et al., 2008). The COD data shown in Fig. 7c confirm the formation of stable by-products, leading to the incomplete total mineralization.
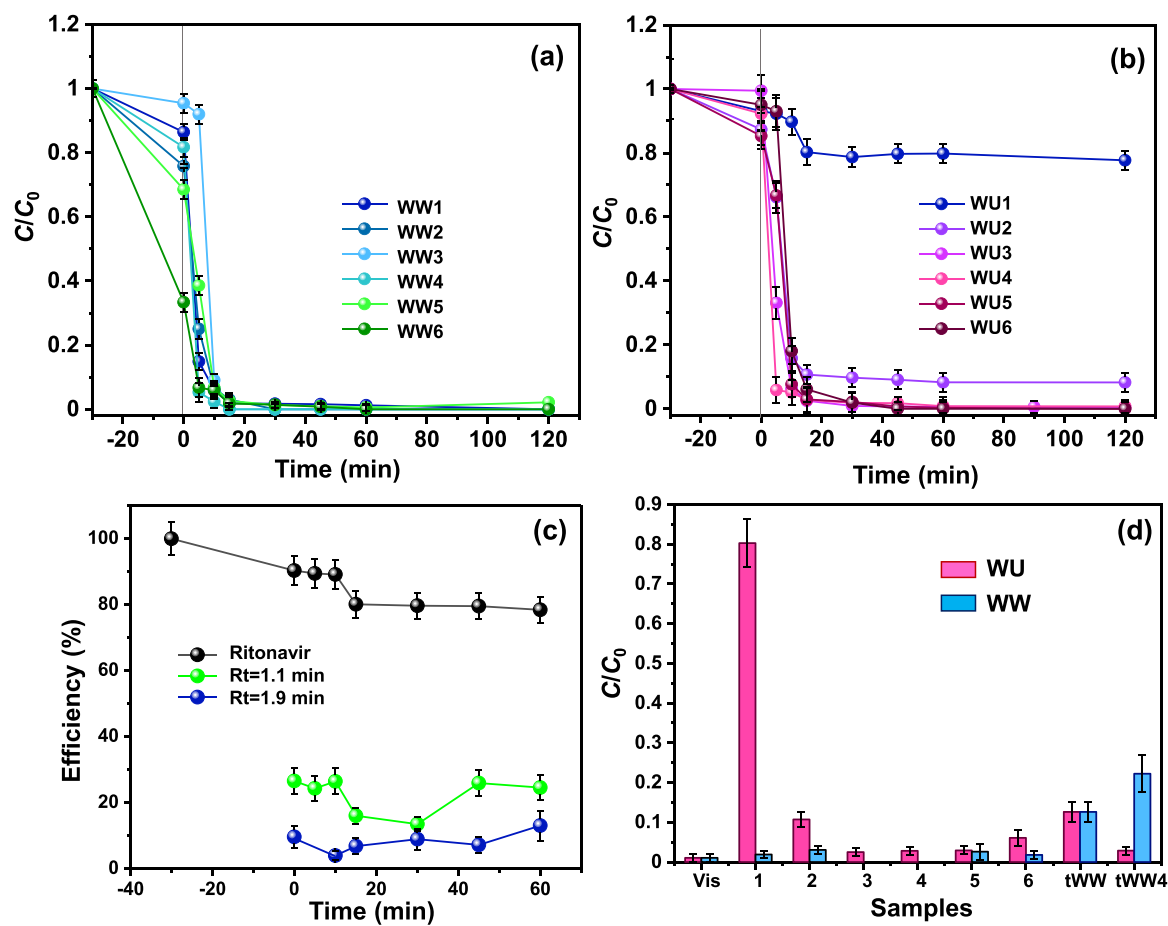
Multiphase photocatalyst + hv → multiphase photocatalyst + e⁻ + h⁺   (9)
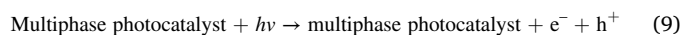
e⁻ + O$_2$ → O$_2$$^{•-}$ (10)

h⁺ + 2H$_2$O → •OH + H⁺   (11)

Fig. 6. Photocatalytic removal of ritonavir by (a) *WW* and (b) *WU* photocatalysts. (c) Efficiency of photocatalytic removal of ritonavir by *WU1* and its photo-degradation products (R_t = 1.1 min and R_t = 1.9 min) and (d) efficiency of photocatalytic removal of ritonavir by *WW* and *WU* photocatalysts after 15 min of irradiation. $C_{0Ritonavir}$ = 10 mg·L^{-1}, $m_{photocatalyst}$ = 0.4 g·L^{-1}, visible light irradiation, *1–6* refer to the order number of *WW* and *WU* photocatalysts.

Fig. 7. Possible photodegradation pathways of ritonavir (a) and lopinavir (b) by the synthesized multiphase photocatalysts. (c) Chemical oxygen demand (COD) of lopinavir- and ritonavir-containing water samples after photocatalytic treatment using *WU* and *WW* photocatalysts.

$$O_2^{\bullet-} + 2H_2O \rightarrow 2\,{}^{\bullet}OH + 2OH^- \qquad (12)$$

$$OH^- + H^+ \rightarrow {}^{\bullet}OH \qquad (13)$$

$$O_2^{\bullet-} + Ritonavir/Lopinavir \rightarrow degradation\ products \qquad (14)$$

$${}^{\bullet}OH + Ritonavir/Lopinavir \rightarrow degradation\ products \qquad (15)$$

3.3.2. Photocatalytic removal of lopinavir in model wastewater

In the photocatalytic removal of lopinavir ($C_{37}H_{48}N_4O_5$, 628.80 g·mol^{-1}, logK_{ow} = 5.94) from model wastewater, all *WW* photocatalysts were effective (Fig. 8a). After 15 min of irradiation, direct photolysis removed about 80% of lopinavir. However, traces of lopinavir were found in model wastewater after 90 min of irradiation, suggesting that lopinavir is less susceptible to solar-driven degradation. The total decomposition of lopinavir is achieved after the photocatalytic treatment using *WW* photocatalysts for 15–20 min. In contrast, in the

Fig. 8. Photocatalytic removal of lopinavir by (a) *WW* and (b) *WU* photocatalysts. (c) Efficiency of photocatalytic removal of lopinavir by *WW* and *WU* photo-catalysts after 15 min: $C_{0Lopinavir} = 10$ mg·L^{-1}, $m_{photocatalyst} = 0.4$ g·L^{-1}, visible light irradiation, *1–6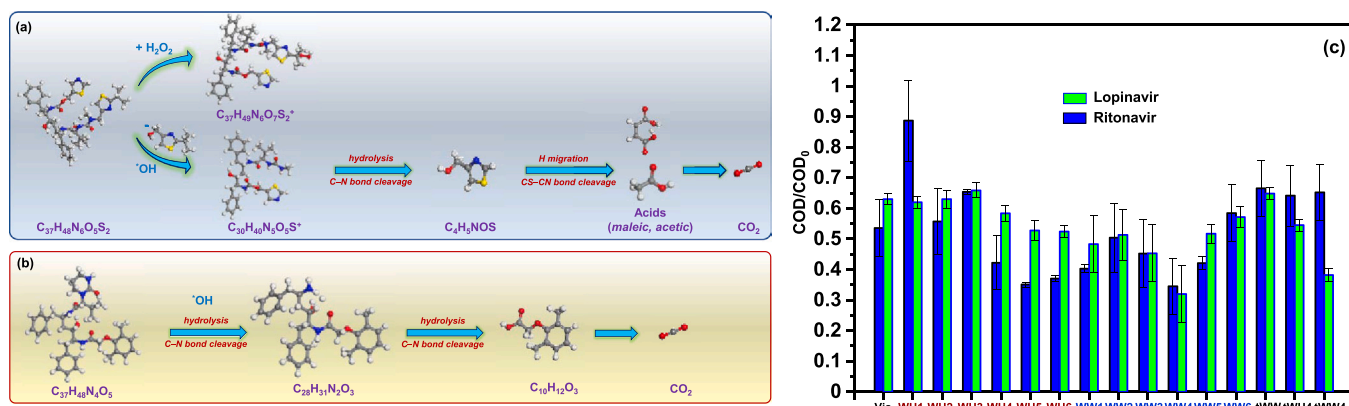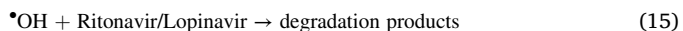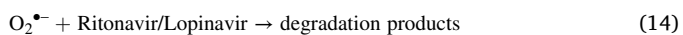* refe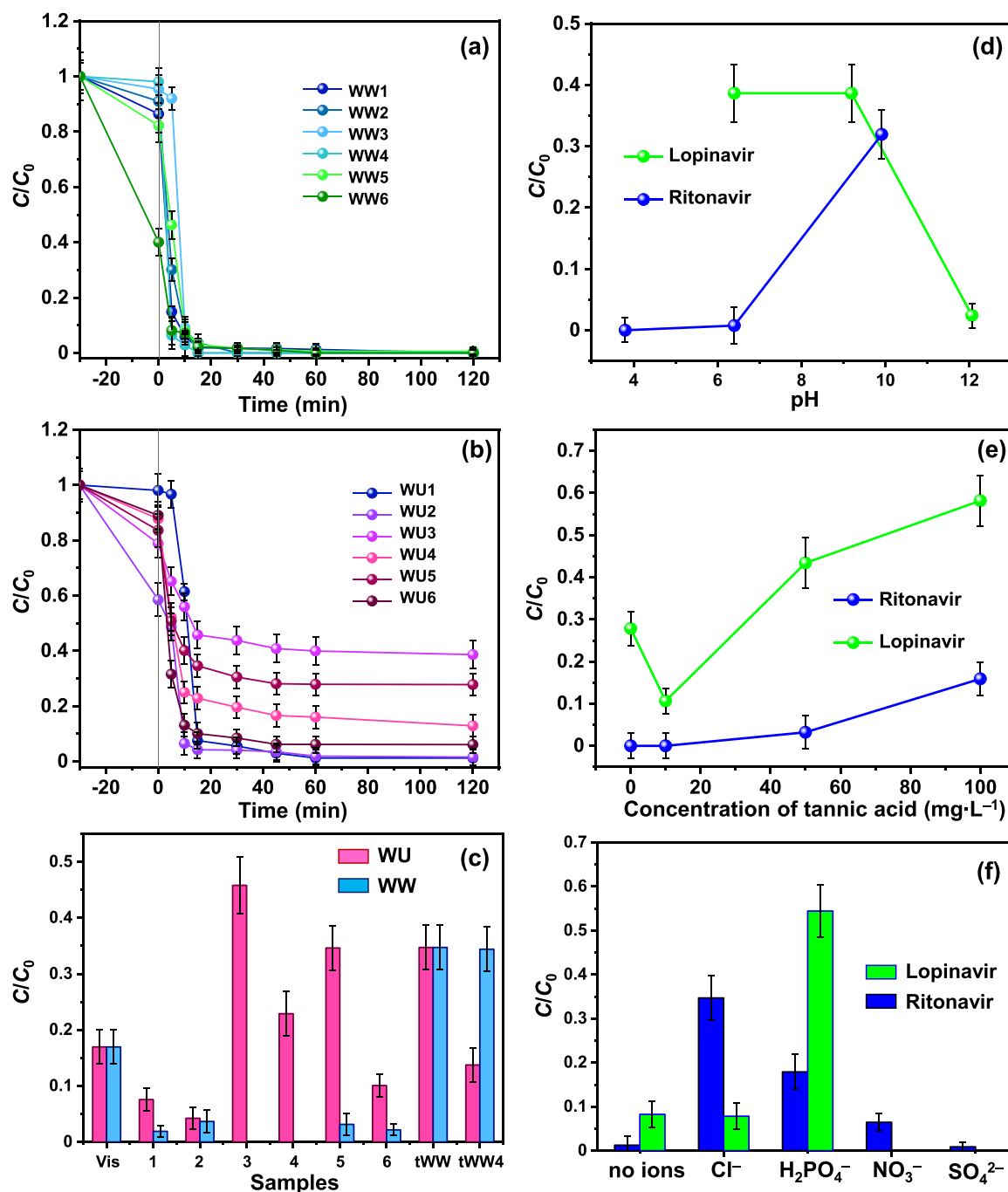r to the order number of *WW* and *WU* photocatalysts. Effects of various parameters on photocatalytic removal efficiency of ritonavir and lopinavir by *WU4*: (d) pH, (e) DOM, and (f) inorganic ions ($C_0 = 5 \times 10^{-3}$ M).

photocatalytic removal of lopinavir, the effectiveness of *WU* photo-catalysts was reduced (Fig. 8b). Direct photolysis was outperformed only by the *WU1* and *WU2*. When the photocatalytic removal efficiency of lopinavir from model wastewater is compared after 15 min of irradiation (Fig. 8c), it is obvious that the *WU1, WU2, WU6*, and all *WW* photocatalysts are more efficient. Previously, a similar trend was observed for the photocatalytic removal of zanamivir (antiviral drug) (Woche et al., 2016) when the addition of photocatalyst (TiO$_2$) was responsible for the transformation of the reaction mechanism, which was completely distinct from the photolytic reaction.

3.3.3. Effects of various parameters on photocatalytic removal efficiency of ritonavir and lopinavir in model wastewater

The pH-, dissolved organic matter (DOM)-, and competing inorganic ions-dependent experiments were conducted using only *WU4* photo-catalyst to investigate the factors affecting the photocatalytic removal efficiency of antiviral drugs. As shown in Fig. 8d, an increase in the pH value decreases the photocatalytic removal efficiency of ritonavir while increasing the photocatalytic removal efficiency of lopinavir. At pH below pKa, lopinavir is present in its non-dissociated form as a strong base. Because the surfaces of the synthesized multiphase photocatalysts are acidic (pH$_{PZC}$ = 9.85 for *WW6* and 10.24 for *WU6*), the obtained results are consistent with the surface charge measurements. This

further hampered the adsorption and photocatalytic degradation of ritonavir and lopinavir. The hydrophobic properties of the tested compounds ($\log K_{ow} > 4$) may imply that they have a higher bioaccumulation potential.

As expected, the photocatalytic removal efficiency of ritonavir and lopinavir was reduced when dissolved organic matter (e.g., tannic acid) was present (Fig. 8e). On the other hand, the impact was slightly linear ($R_{lopinavir}^2 = 0.89$ and $R_{ritonavir}^2 = 0.96$). The photocatalytic removal efficiency of lopinavir was dramatically increased from 70% to 90% when a small amount of tannic acid was added to the aqueous solution containing lopinavir (Wang et al., 2014). Possibly, tannic acid may have served as a complexing agent. Tannic acid acted as a superoxide anion or hydrogen peroxide radical scavenger at higher concentrations (Gülçin et al., 2010), lowering the photocatalytic removal efficiency of lopinavir. The introduction of certain inorganic ions altered the photocatalytic removal efficiency of lopinavir, as shown in Fig. 8f. The presence of Cl^-, NO_3^-, or SO_4^{2-} had no effect on the photocatalytic removal efficiency of lopinavir, and only $H_2PO_4^-$ hampered photocatalytic oxidation. The highest reduction in the photocatalytic removal efficiency of ritonavir was observed when Cl^- was introduced, and both $H_2PO_4^-$ and NO_3^- similarly reduced the photocatalytic removal efficiency of ritonavir.

The photocatalytic removal of ritonavir and lopinavir was mediated by radicals (Fig. A.3a), and the photocatalytic removal efficiency of both antiviral drugs by *WU1* was reduced in the presence of radical scavengers. It can be seen that PBQ as an $O_2^{\bullet-}$ scavenger had the greatest effect on the removal of ritonavir. The most prevalent form of oxygen species was $O_2^{\bullet-}$ (pKa of reaction: $HO_2^{\bullet} \leftrightarrow O_2^{\bullet-} + H^+$ is 4.8 ± 0.1) due to slightly acidic reaction conditions (pH~6.4) (Cavalcante et al., 2016). The effect of holes was noted as the photocatalytic removal efficiency of ritonavir was reduced in the presence of 2Na-EDTA (Gunture et al., 2019). The $\bullet$OH radicals were also shown by the minor effect. The other pathway for the photocatalytic removal of lopinavir was identified. IPA had the most suppressive impact, followed by PBQ and 2Na-EDTA, showing that $O_2^{\bullet-} > {}^{\bullet}OH \sim h^+$ has the greatest effect. IPA is considered as $\bullet$OH scavenger, with a reaction rate constant of $2 \times 10^9 \, M^{-1} \, s^{-1}$ (Rodríguez et al., 2015). On the other hand, when IPA reacts with h^+, it can behave as an electron donor (Cavalcante et al., 2016). The significantly reduced removal efficiency in the presence of 2Na-EDTA (a scavenger of h^+) suggests that both $\bullet$OH and h^+ were important in the photocatalytic oxidation of lopinavir on the *WU1* surface. According to the results of recyclability test conducted using *WU6*, the effectiveness of the synthesized multiphase photocatalyst showed a slight decrease after the third cycle, indicating their good stability (Fig. A.3b). In the bisphenol AF degradation by $FeMoO_4$ (Wang et al., 2021), a similar effect of $\bullet$OH and non-radical singlet oxygen - $^1[O_2]$ was observed. The generation of surface $O_2^{\bullet-}$ was favored by the presence of more oxygen vacancies in $FeMoO_4$ (Zhang et al., 2011). $MgWO_4$ (Bhuyan et al., 2017), like in the *WW* photocatalysts, had more active photocatalytic or Lewis acid sites, and the effect of $O_2^{\bullet-}$ on the photocatalytic dye removal was noted (Gouveia et al., 2020). Also, $\bullet$OH was found to be the most reactive species generated when WO_3 was irradiated (Nisar et al., 2020).

3.3.4. Photocatalytic removal of antiviral drugs in real wastewater

The main route for lopinavir and ritonavir to enter the environment is through wastewater. Up to 22% and 37% of unmetabolized lopinavir and ritonavir are excreted with faces, respectively (Kuroda et al., 2021). This may result in the emergence of antiviral drug-resistant virus strains within the bodies of select wild animals (Kuroda et al., 2021). Therefore, the photocatalytic removal of lopinavir and ritonavir in real treated wastewater (tWW) was assessed using the synthesized multiphase photocatalysts. Direct photolysis of ritonavir in model wastewater was fast but slowed in the presence of additional water components, as shown in Fig. A.4a. After 45 min of direct irradiation of tWW with a high dosage of ritonavir, 90% photocatalytic removal efficiency was reached. In the presence of *WU4* and *WW4* photocatalysts, the photocatalytic removal process was very efficient, and 95% ritonavir was removed after 15 min

of irradiation. In both model and real treated wastewaters, lopinavir demonstrated a decreased susceptibility to photocatalytic removal (Fig. A.4b). Also, lopinavir was more efficiently removed using the photocatalytic oxidation of tWW than direct photolysis. Interestingly, when the *WW4* was used, the first 45 min of irradiation resulted in a lower susceptibility to irradiation. However, lopinavir was successfully removed after 60 min of irradiation, with a residual concentration of lopinavir of less than 5%. According to Kovalova et al. (2013), the post-treatment of hospital wastewater with powdered activated carbon was effective, removing more than 90% of ritonavir. The presence of tWW components, such as bicarbonates and DOM, is linked to the highest removal rate in tWW. The removal rates for $\bullet$OH and CO_3^{2-} (estimated to be $8.5 \cdot 10^6 \, L \, mol^{-1} \, s^{-1}$) are significantly higher than the reaction rates of $\bullet$OH. Particularly, the DOM played two different roles: (i) radical scavenger and (ii) radical chain promoter (Zwiener and Frimmel, 2000).

3.3.5. Kinetics

Three well-known models were used to determine the kinetics of the photocatalytic oxidation of lopinavir and ritonavir by the synthesized multiphase photocatalysts: zero-order, first-order, and second-order (Ahmed and Emam, 2020). Table A.1 shows the rate constant k, half time $T_{1/2}$, and correlation coefficient R^2. The Chi-squared test (χ^2) was used to determine the statistical characteristics of kinetics data (Ahmed et al., 2021). The first-order regime has the highest R^2 and the lowest χ^2 values, indicating that this kinetics model best fits the experimental data (Zhang et al., 2011; Ahmed et al., 2020). The kinetics of the photocatalytic removal of lopinavir and ritonavir in model and real treated wastewaters by the synthesized multiphase photocatalysts followed a pseudo-first-order regime (Ahmed and Emam, 2019; Zhang et al., 2019).

The k_1 values observed for the photocatalytic removal of ritonavir were higher than that observed for the photocatalytic removal of lopinavir (Table 1). When the *WU* photocatalysts were used, the difference was one order of magnitude greater. The highest k_1 value was observed during the photocatalytic removal of ritonavir from model wastewater by *WW4* ($35.64 \times 10^{-2} \, min^{-1}$). The obtained values for the photocatalytic removal of lopinavir by *WU* photocatalysts are consistent with the k_1 values obtained by Wang et al. (2015) during the photocatalytic removal of Tamiflu (an antiviral drug) by P25-TiO$_2$ under UV-A irradiation ($0.040 \, min^{-1}$). The k_1 values obtained using the *WU* photocatalysts for the photocatalytic removal of ritonavir and the *WW* photocatalysts for the photocatalytic removal of lopinavir and ritonavir are significantly higher than those obtained using pure anatase photocatalyst ($k_1 =$

Table 1
Kinetics of the photocatalytic removal of lopinavir and ritonavir from model and real wastewaters by *WU* and *WW* photocatalysts.

Sample	k_1 (min^{-1}) $\times$ 100 lopinavir	R^2	k_1 (min^{-1}) $\times$ 100 ritonavir	R^2
Vis	4.20	0.8805	30.49	0.9997
WU in model wastewater				
WU1	3.82	0.6732	0.94	0.7945
WU2	4.81	0.7756	15.46	0.9241
WU3	0.48	0.5500	5.84	0.8587
WU4	1.21	0.5458	21.22	0.7748
WU5	0.65	0.4436	24.57	0.9246
WU6	1.59	0.439841	19.78	0.9038
WW in model wastewater				
WW1	5.48	0.6132	24.76	0.9806
WW2	21.96	0.9899	21.99	0.9900
WW3	23.50	0.7617	23.58	0.7877
WW4	35.32	0.9091	35.64	0.9191
WW5	7.12	0.7914	23.11	0.9665
WW6	6.80	0.8864	7.14	0.9162
in real treated wastewater				
in tWW	2.40	0.7762	14.01	0.9902
WW4 in tWW	4.36	0.9130	6.93	0.9649
WU4 in tWW	3.74	0.7911	22.52	0.9746

0.0034–0.0072 min^{-1}).

According to Kisch and Bahnemann (2015), the reaction rates for the photocatalytic systems based on suspensions of semiconductor powders in dissolved substrates are adequate for comparison. The reaction rates must, however, be measured using the same type of photoreactor under identical irradiation conditions, and the intensity of the incident light must be integrated in the same wavelength range. Finding the most appropriate experimental data that satisfy the above criteria is difficult. Therefore, the photocatalytic performance was compared using the order of magnitude of the pseudo-first-order kinetic constants (k_1). Thi et al. (2021) recently compiled the experimental data on the photocatalytic degradation of selected antiviral drugs that had been published so far. It should be mentioned that under UV irradiation at 365 nm and using P25-TiO$_2$ photocatalyst, pseudo-first-order kinetic constants (k_1) have been reported (Thi et al., 2021) in magnitudes comparable to those obtained in this study for the photocatalytic removal of lopinavir and ritonavir by the synthesized multiphase photocatalysts (Table 1). Previously, 0.040 min^{-1} at 1.8 mW•cm^{-2} irradiance was reported for the photocatalytic removal of oseltamivir (Wang et al., 2015), and 0.0263 (An et al., 2015b), 0.0542 (An et al., 2011), 0.076 (An et al., 2015a), 0.084 (An et al., 2015a), and 0.102 (An et al., 2015a) min^{-1} were obtained for the photocatalytic removal of acyclovir, lamivudine, 1-amantadine, 2-amantadine, and rimantadine, respectively, at 0.36 mW•cm^{-2} irradiance. Therefore, the k_1 values obtained for the photocatalytic removal of ritonavir by *WU* photocatalysts and for the photocatalytic removal of lopinavir and ritonavir by *WW* photocatalysts are significantly higher than those obtained using pure anatase photocatalyst.

3.4. Ecotoxicity

In general, the effect of the photocatalytic treatment is evaluated in terms of the removal efficiency of a target pollutant. However, some toxic by-products or products of the photocatalytic oxidation of the target pollutant can also be generated during photocatalytic treatment,

which are potentially harmful to the environment and human beings (Calza et al., 2006). Therefore, a different method must be applied for the assessment of the effectiveness of photocatalytic treatment in detoxifying the water samples containing antiviral drugs, pharmaceuticals, and other emerging pollutants. The bioconcentration factor is used as an indication for predicting bioaccumulation in living organisms. According to the bioconcentration factors (1.32 L•kg^{-1} ritonavir and >1 L•kg^{-1} lopinavir) (Kumari and Kumar, 2021), both antiviral drugs may accumulate in the fish body more than in the surrounding water. There are few studies on the effects of tested compounds on living organisms; however, some modeling studies (Kuroda et al., 2021; Kumari and Kumar, 2021) have predicted that ritonavir and lopinavir may have high chronic toxicity (narcosis) to aquatic organisms due to their high hydrophobicity (PNEC 2.9 ng•L^{-1} for ritonavir and PNEC 4.7 ng•L^{-1} for lopinavir). Furthermore, their metabolites have high toxicity (Kuroda et al., 2021), suggesting that additional wastewater treatment or on-site pretreatment (e.g., ozonation, oxidation, etc.) is required to effectively remove antiviral drugs and pharmaceuticals.

The collected ecotoxicity data show that the variations in *Danio rerio* can be observed in the 75% diluted tWW solution (Fig. 9a and b). The length of *Danio rerio* was not altered, but organogenesis was disrupted. The presence of lopinavir in the tWW (Fig. 9c) had an effect on fish embryo mortality; however, no dead fish embryos were found. On the other hand, the length of *Danio rerio* was reduced up to 40%. Surprisingly, when lopinavir-containing tWW was contacted with fish embryos after photocatalytic treatment using *WW4*, a 100% mortality rate was noted after exposure to undiluted tWW (100%). The modifications in the fish morphology were observed in the 75% diluted tWW solution (scoliosis). Although no lopinavir was found in the sample, its intermediates or by-products could be harmful to fish. This implies that when advanced oxidation processes are applied to treat real environmental samples, estimating only one parameter - the decreased concentration of the target pollutant – is insufficient, and the final ecotoxicity of photocatalytically treated water samples must be
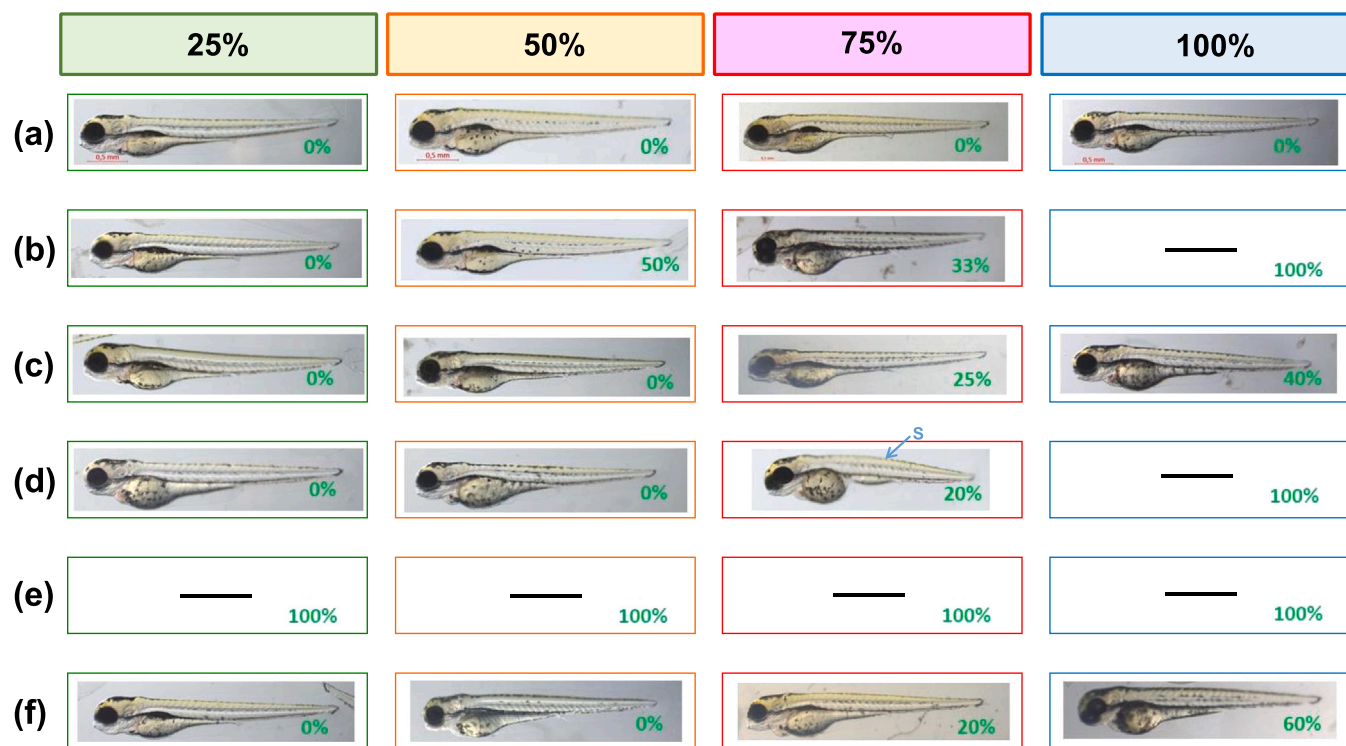
Fig. 9. Mortality rate and developmental malformations of *Danio rerio* exposed to wastewater samples containing lopinavir or ritonavir: (a) E3 – control, (b) tWW, (c) lopinavir-containing tWW before photocatalytic treatment, (d) lopinavir-containing tWW after photocatalytic treatment using *WW4*, (e) ritonavir-containing tWW before photocatalytic treatment, and (f) ritonavir-containing tWW after photocatalytic treatment using *WW4*. S – scoliosis.

assessed. Also, Kumari and Kumar (2021) pointed out that priority pollutants in wastewater effluents must be regularly monitored before discharging them into rivers, lakes, and open water reservoirs. As shown in Fig. 9e, the presence of ritonavir in tWW was lethal to *Danio rerio*. The developed multiphase photocatalysts effectively reduced the toxicity of model and real wastewaters containing ritonavir during photocatalytic treatment (Fig. 9f). According to the number of survived embryos (100%), the application of photocatalytic treatment using the developed multiphase photocatalysts was successful in achieving water with no toxicity, and it is an effective method for removing various toxic chemicals from contaminated water with low ecotoxicity.

4. Conclusions

In summary, multiphase photocatalysts were synthesized by a simple calcination of industrial waste from ammonium molybdate production (*WU* photocatalysts) and its combination with WO$_3$ (*WW* photocatalysts). The XRD results showed that Fe$_3$O$_4$, Fe$_2$O$_3$, MgMoO$_4$, FeMoO$_4$, and MgFeAlO$_4$ crystalline phases were dominant in the *WU* photocatalysts, and Fe$_2$O$_3$, FeWO$_4$, MgWO$_4$, and Fe$_2$Mo$_3$O$_{12}$ crystalline phases were prevalent in the *WW* photocatalyst. The *WU* and *WW* photocatalysts could absorb visible light up to 620 nm due to the presence of visible-light-active crystalline phases. Effects of calcination temperature of industrial waste (550–950 °C) and WO$_3$ content (0–100%) on photocatalytic activity of multiphase photocatalysts (*WU* and *WW*) for efficient removal of SARS-CoV-2 antiviral drugs (lopinavir and ritonavir) in model and real wastewaters were studied. The highest k_1 value was observed for the photocatalytic removal of ritonavir from model wastewater using *WW4* (35.64 $\times10^{-2}$ min^{-1}). The synthesized multiphase photocatalysts exhibited 95% efficiency in the photocatalytic removal of ritonavir within 15 min of visible light irradiation. In contrast, 60 min of visible light irradiation was necessary to achieve 95% efficiency in the photocatalytic removal of lopinavir. The ecotoxicity test conducted using zebrafish (*Danio rerio*) embryos showed no toxicity for photocatalytically treated ritonavir-containing wastewater, and the contrary trend was observed for photocatalytically treated lopinavir-containing wastewater. The synthesized multiphase photocatalysts can also be tested and applied for degradation of other SARS-CoV-2 antiviral drugs in wastewater. The current study demonstrated a simple route for turning the industrial waste from ammonium molybdate production into useful photocatalytic materials for removal of SARS-CoV-2 antiviral drugs.

CRediT authorship contribution statement

Bożena Czech: Investigation, Methodology, Visualization, Writing – original draft, Conceptualization, Validation, Supervision; **Anna Wasilewska:** Investigation; **Anna Boguszewska-Czubara:** Investigation, Methodology, Visualization; **Kunio Yubuta:** Investigation, Writing – review & editing; **Hajime Wagata:** Investigation, Writing – review & editing; **Shahlo S. Daminova:** Investigation, Writing – review & editing; **Zukhra C. Kadirova:** Investigation, Writing – review & editing; **Ronald Vargas:** Investigation, Writing – original draft; **Mirabbos Hojamberdiev:** Investigation, Methodology, Visualization, Writing – review & editing, Conceptualization, Resources, Supervision.

Declaration of Competing Interest

The authors declare that they have no known competing financial interests or personal relationships that could have appeared to influence the work reported in this paper.

Appendix A. Supporting information

Supplementary data associated with this article can be found in the online version at doi:10.1016/j.jhazmat.2022.128300.

References

Abafe, O.A., Späth, J., Fick, J., Jansson, S., Buckley, C., Stark, A., Pietruschka, B., Martincigh, B.S., 2018. LC-MS/MS determination of antiretroviral drugs in influents and effluents from wastewater treatment plants in KwaZulu-Natal, South Africa. Chemosphere 200, 660–670.

Ahmed, H.B., Emam, H.E., 2019. Synergistic catalysis of monometallic (Ag, Au, Pd) and bimetallic (Ag-Au, Au-Pd) versus trimetallic (Ag-Au-Pd) nanostructures effloresced via analogical techniques. J. Mol. Liq. 287, 110975.

Ahmed, H.B., Emam, H.E., 2020. Seeded growth core-shell (Ag–Au–Pd) ternary nanostructure at room temperature for potential water treatment. Polym. Test. 89, 106720.

Ahmed, H.B., Mikhail, M.M., El-Sherbiny, S., Nagy, K.S., Emam, H.E., 2020. pH responsive intelligent nano-engineer of nanostructures applicable for discoloration of reactive dyes. J. Colloid Interface Sci. 561, 147–161.

Ahmed, H.B., Saad, N., Emam, H.E., 2021. Recyclable palladium based nano-catalytic laborer encaged within bio-granules for dye degradation. Surf. Interfaces 25, 101175.

An, J., Li, G., An, T., Song, W., Feng, H., Lu, Y., 2015a. Photocatalytic degradation of three amantadine antiviral drugs as well as their eco-toxicity evolution. Catal. Today 258, 602–609.

An, T., An, J., Yang, H., Li, G., Feng, H., Nie, X., 2011. Photocatalytic degradation kinetics and mechanism of antivirus drug-lamivudine in TiO$_2$ dispersion. J. Hazard. Mater. 197, 229–236.

An, T., An, J., Gao, Y., Li, G., Fang, H., Son, W., 2015b. Photocatalytic degradation and mineralization mechanism and toxicity assessment of antivirus drug acyclovir: experimental and theoretical studies. Appl. Catal. B 164, 279–287.

Bedoya-Lora, F.E., Holmes-Gentle, I., Hankin, A., 2021. Electrochemical techniques for photoelectrode characterization. Curr. Opin. Green Sustain. Chem. 29, 100463.

Bhembe, Y.A., Lukhele, L.P., Hlekelele, L., Ray, S.S., Sharma, A., Vo, D.V.N., Dlamini, L.N., 2020. Photocatalytic degradation of nevirapine with a heterostructure of few-layer black phosphorus coupled with niobium (V) oxide nanoflowers (FL-BP@ Nb2O5). Chemosphere 261, 128159.

Bhosale, R., Jain, S., Vinod, C.P., Kumar, S., Ogale, S., 2019. Direct Z-scheme g-C$_3$N$_4$/FeWO$_4$ nanocomposite for enhanced and selective photocatalytic CO$_2$ reduction under visible light. ACS Appl. Mater. Interfaces 11, 6174–6183.

Bhuyan, P.D., Singh, D., Kansara, S., Yadav, P., Gupta, S.K., Sonvane, Y., Rout, S.K., Sinha, E., 2017. Experimental and theoretical analysis of electronic and optical properties of MgWO$_4$. J. Mater. Sci. 52, 4934–4943.

Broda, E., Gładysz-Płaska, A., Skwarek, E., Payentko, V.V., 2021. Structural properties and adsorption of uranyl ions on the nanocomposite hydroxyapatite/white clay. Appl. Nanosci. https://doi.org/10.1007/s13204-021-01790-y.

Brown, L.A.K., Freemantle, N., Breuer, J., Dehbi, H.M., Chowdhury, K., Jones, G., Ikeji, F., Ndoutoumou, A., Santhirakumar, K., Longley, N., Checkley, A.M., Standing, J.F., Lowe, D.M., 2021. Early antiviral treatment in outpatients with COVID-19 (FLARE): a structured summary of a study protocol for a randomised controlled trial. Trials 22, 193.

Calza, P., Sakkas, V.A., Medana, C., Baiocchi, C., Dimou, A., Pelizzetti, E., Albanis, T., 2006. Photocatalytic degradation study of diclofenac over aqueous TiO$_2$ suspensions. Appl. Catal. B Environ. 67, 197–205.

Cavalcante, R.P., Dantas, R.F., Bayarri, B., González, O., Giménez, J., Esplugas, S., Machulek Junior, A., 2016. Photocatalytic mechanism of metoprolol oxidation by photocatalysts TiO$_2$ and TiO$_2$ doped with 5% B: primary active species and intermediates. Appl. Catal. B 194, 111–122.

Chitturi, S.R., Bharathi, Ch, Reddy, A.V.R., Ch. Reddy, K., Sharma, H.K., Handa, V.K., Dandala, R., Bindu, V.H., 2008. Impurity profile study of lopinavir and validation of HPLC method for the determination of related substances in lopinavir drug substance. Pharm. Biomed. Anal. 48, 1430–1440.

Choudhary, J., Dheeman, S., Sharma, V., Katiyar, P., Karn, S.K., Sarangi, M.K., Chauhan, A.K., Verma, G., Baliyan, N., 2021. Insights of Severe Acute Respiratory Syndrome Coronavirus (SARS-CoV-2) pandemic: a current review. Biol. Proced. Online 23, 5.

Corby, S., Pastor, E., Dong, Y., Zheng, Z., Francas, L., Sacha, M., Kafizas, S.A., Bakulin, A., Durrant, J., 2019. Charge separation, band-bending and recombination in WO$_3$ photoanodes. J. Phys. Chem. Lett. 10, 5395–5401.

Costa, G.S., Costa, M.J.S., Oliveira, H.G., Lima, L.C.B., Luz Jr., G.E., Cavalcante, L.S., Santos, R.S., 2020. Effect of the applied potential condition on the photocatalytic properties of Fe$_2$O$_3$/WO$_3$ heterojunction films. J. Inorg. Organomet. Polym. Mater. 30, 2851–2862.

Czech, B., Zygmunt, P., Kadirova, Z.C., Yubuta, K., Hojamberdiev, M., 2020. Effective photocatalytic removal of selected pharmaceuticals and personal care products by elsmoreite/tungsten oxide@ZnS photocatalyst. J. Environ. Manag. 270, 110870.

Donato, M., Dias, C.L., Rossi, R.C., Valente, R.S., Fröehlich, P.E., Bergold, A.M., 2006. LC method for studies on the stability of lopinavir and ritonavir in soft gelatin capsules. Chromatographia 63, 437–443.

Gomis-Berenguer, A., Iniesta, J., Fermín, D.J., Ania, C.O., 2018. Photoelectrochemical response of WO₃/nanoporous carbon anodes for photocatalytic water oxidation. C J. Carbon Res. 4, 45.

Gouveia, A.F., Vieira, V.E.M., Sczancoski, J.C., Lemos, P.S., Rout, S.K., Arul, N.S., Longo, E., Cavalcante, L.S., 2020. Electronic structure, morphological aspects, and photocatalytic discoloration of three organic dyes with MgWO₄ powders synthesized by the complex polymerization method. J. Inorg. Organomet. Polym. Mater. 30, 2952–2970.

Gülçin, I.I., Huyut, Z., Elmastaş, M., Aboul-Enein, H.Y., 2010. Radical scavenging and antioxidant activity of tannic acid. Arab. J. Chem. 3, 43–53.

Gunture, Singh, A., Bhati, A., Khare, P., Tripathi, K.M., Sonkar, S.K., 2019. Soluble graphene nanosheets for the sunlight-induced photodegradation of the mixture of dyes and its environmental assessment. Sci. Rep. 9, 2522.

Guo, J., Gan, Z., Lu, Z., Liu, J., Xi, J., Wan, Y., Le, L., Liu, H., Shi, J., Xiong, R., 2013. Improvement of the photocatalytic properties of TiO₂ by (Fe+Mo) co-doping—a possible way to retard the recombination process. J. Appl. Phys. 114, 104903–104910.

Hibino, T., Tsunashima, A., 1997. Synthesis of paramolybdate intercalates of hydrotalcite-like compounds by ion exchange in ethanol/water solution. Chem. Mater. 9, 2082–2089.

Hojamberdiev, M., Cai, Y., Vequizo, J.J.M., Khan, M.M., Vargas, R., Yubuta, K., Yamakata, A., Teshima, K., Hasegawa, M., 2018. Binary flux-promoted formation of trigonal ZnIn₂S₄ layered crystals using ZnS-containing industrial waste and their photocatalytic performance for H₂ production. Green Chem. 20, 3845–3856.

Hojamberdiev, M., Piccirillo, C., Cai, Y., Kadirova, Z.C., Yubuta, K., Ruzimuradov, O., 2019. ZnS-containing industrial waste: antibacterial activity and effects of thermal treatment temperature and atmosphere on photocatalytic activity. J. Alloy. Compd. 791, 971–982.

Hojamberdiev, M., Goel, N., Kumar, R., Kadirova, Zukhra C., Kumar, M., 2020a. Efficient NO₂ sensing performance of a low-cost nanostructured sensor derived from molybdenite concentrate. Green Chem. 22, 6981–6991.

Hojamberdiev, M., Czech, B., Göktaş, A.C., Yubuta, K., Kadirova, Z.C., 2020b. SnO₂@ZnS photocatalyst with enhanced photocatalytic activity for the degradation of selected pharmaceuticals and personal care products in model wastewater. J. Alloy. Compd. 827, 154339.

Hojamberdiev, M., Vargas, R., Bhati, V.S., Torres, D., Kadirova, Z.C., Kumar, M., 2021. Unraveling the photoelectrochemical behavior of Ni-modify ZnO and TiO₂ thin films fabricated by RF magnetron sputtering. J. Electroanal. Chem. 882, 115009.

Ibhadon, A.O., Fitzpatrick, P., 2013. Heterogeneous photocatalysis: recent advances and applications. Catalysts 3, 189–218.

Jain, S., Kumar, P., Vyas, R.K., Pandit, P., Dalai, A.K., 2013. Occurrence and removal of antiviral drugs in environment: a review. Water Air Soil Pollut. 224, 1410.

Kavitha, V., Palanivelu, K., 2004. The role of ferrous ion in Fenton and photo-Fenton processes for the degradation of phenol. Chemosphere 55, 1235–1243.

Kisch, H., Bahnemann, D., 2015. Best practice in photocatalysis: comparing rates or apparent quantum yields? J. Phys. Chem. Lett. 6, 1907–1910.

Kopinke, F.-D., Georgi, A., 2017. What controls selectivity of hydroxyl radicals in aqueous solution? Indications for a cage effect. J. Phys. Chem. A 121, 7947–7955.

Kosma, C.I., Nannou, C.I., Boti, V.I., Albanis, T.A., 2019. Psychiatrics and selected metabolites in hospital and urban wastewaters: occurrence, removal, mass loading, seasonal influence and risk assessment. Sci. Total Environ. 659, 1473–1483.

Kou, S.B., Zhou, K.L., Lin, Z.Y., Lou, Y.Y., Shi, J.H., Liu, Y.X., 2021. Insights into the binding properties of calf thymus DNA with lopinavir from spectroscopic and computational studies. J. Mol. Liq. 328, 115491.

Kovalova, L., Siegrist, H., Von Gunten, U., Eugster, J., Hagenbuch, M., Wittmer, A., Moser, R., McArdell, C.S., 2013. Elimination of micropollutants during post-treatment of hospital wastewater with powdered activated carbon, ozone, and UV. Environ. Sci. Technol. 47, 7899–7908.

Kumari, M., Kumar, A., 2021. Can pharmaceutical drugs used to treat Covid-19 infection leads to human health risk? A hypothetical study to identify potential risk. Sci. Total Environ. 778, 146303.

Kuroda, K., Li, C., Dhangar, K., Kumar, M., 2021. Predicted occurrence, ecotoxicological risk and environmentally acquired resistance of antiviral drugs associated with COVID-19 in environmental waters. Sci. Total Environ. 776, 145740.

Li, F., Jian, J., Xu, Y., Wang, S., Wang, H., Wang, H., 2021. Recent advances on interfacial engineering of hematite photoanodes for viable photo-electrochemical water splitting. Eng. Rep. 3, e12387.

Li, G., Nie, X., Gao, Y., An, T., 2016. Can environmental pharmaceuticals be photocatalytically degraded and completely mineralized in water using g-C₃N₄/TiO2 under visible light irradiation?—Implications of persistent toxic intermediates. Appl. Catal. B 180, 726–732.

Li, J., Xiao, C., Wang, K., Li, Y., Zhang, G., 2019. Enhanced generation of reactive oxygen species under visible light irradiation by adjusting the exposed facet of FeWO₄ nanosheets to activate oxalic acid for organic pollutant removal and Cr(VI) reduction. Environ. Sci. Technol. 53, 11023–11030.

Liu, Z., Wu, B., Zhu, Y., Yin, D., Wang, L., 2012. Fe-ions modified BiOBr mesoporous microspheres with excellent photocatalytic property. Catal. Lett. 142, 1489–1497.

Low, J., Yu, J., Jaroniec, M., Wageh, S., Al-Ghamdi, A.A., 2017. Heterojunction photocatalysis. Adv. Mater. 29, 1601694.

Miyazaki, J., Takiyama, H., Nakata, M., 2017. Isocyano compounds newly recognized in photochemical reaction of thiazole: matrixisolation FT-IR and theoretical studies. RSC Adv. 7, 4960–4974.

Monllor-Satoca, D., Díez-García, M.I., Lana-Villareal, T., Gómez, R., 2020. Photoelectrocatalytic production of solar fuels with semiconductor oxides: materials, activity and modeling. Chem. Comm. 56, 12272–12289.

Mosquera-Sulbaran, J.A., Hernández-Fonseca, H., 2021. Tetracycline and viruses: a possible treatment for COVID-19? Arch. Virol. 166, 1–7.

Muller, A., Kondofersky, I., Folger, A., Fattakhova-Rohlfing, D., Bein, T., Scheu, Ch, 2017. Dual absorber Fe₂O₃/WO₃ host-guest architectures for improved charge generation and transfer in photoelectrochemical applications. Mater. Res. Express 4, 016409.

Nannou, C., Ofrydopoulou, A., Evgenidou, E., Heath, D., Heath, E., Lambropoulou, D., 2020. Antiviral drugs in aquatic environment and wastewater treatment plants: a review on occurrence, fate, removal and ecotoxicity. Sci. Total Environ. 699, 134322.

Ng, C., Iwase, A., Ng, Y.H., Amal, R., 2012. Transforming anodized WO₃ films into visible-light-active Bi₂WO₆ photoelectrodes by hydrothermal treatment. J. Phys. Chem. Lett. 3, 913–918.

Nikolenko, N.V., Kozhevnikov, I.V., Kostyniuk, A.O., Bayahia, H., Kalashnykov, Y.V., 2018. Preparation of iron molybdate catalysts for methanol to formaldehyde oxidation based on ammonium molybdoferrate (II) precursor. J. Saudi Chem. Soc. 22, 372–379.

Nisar, J., Hassan, S., Khan, M.I., Iqbal, M., Nazir, A., Sharif, A., Ahmed, E., 2020. Hetero-structured iron molybdate nanoparticles: synthesis, characterization and photocatalytic application. Int. J. Chem. React. Eng. 18, 20190123.

Núñez, O., Madriz, L., Tatá, J., Carvajal, D., Vargas, R., 2019. Unprecedented large solvent (H₂O vs. D₂O) isotope effect in semiconductor photooxidation. J. Phys. Org. Chem. 32, e3952.

Palmer, S.J., Spratt, H.J., Frost, R.L., 2009. Thermal decomposition of hydrotalcites with variable cationic ratios. J. Therm. Anal. Calorim. 95, 123–129.

Parise, J.B., Yeganeh-Haeri, A., Weidner, D.J., Jorgensen, J.D., Saltzberg, M.A., 1994. Pressure-induced phase transition and pressure dependence of crystal structure in low (α) and (Ca/Al-doped cristobalite. J. Appl. Phys. 75, 1361–1367.

Patil, P.S., Patil, P.R., 1996. Studies on the photoelectrochemical cell formed with WO3 photoanode by using Gartner's model. Bull. Mater. Sci. 19, 651–656.

Peter, L., 2018. Photoelectrochemistry: from basic principles to photocatalysis. In: Schneider, J., Bahnemann, D., Ye, J., Li Puma, G., Dionysious, D. (Eds.), Photocatalysis. Fundamentals and Perspectives. RSC Energy and Environmental Perspectives, Cambridge, pp. 3–28.

Peter, L.M., Walker, A.B., Bein, T., Hfnagel, A.G., Kondofersky, I., 2020. Interpretation of photocurrent transients at semiconductor electrodes: effects of band-edge unpinning. J. Electroanal. Chem. 872, 114234.

Quan, H., Gao, Y., Wang, W., 2020. Tungsten oxide-based visible light-driven photocatalysts: crystal and electronic structures and strategies for photocatalytic efficiency enhancement. Inorg. Chem. Front. 7, 817–838.

Rajagopal, S., Nataraj, D., Khyzhun, O.Y., Djaoued, Y., Robichaud, J., Mangalaraj, D., 2010. Hydrothermal synthesis and electronic properties of FeWO₄ and CoWO₄ nanostructures. J. Alloy. Compd. 493, 340–345.

Rao, R.N., Ramachandra, B., Vali, R.M., Raju, S.S., 2010. LC–MS/MS studies of ritonavir and its forced degradation products. J. Pharm. Biomed. Anal. 53, 833–842.

Rodríguez, E.M., Márquez, G., Tena, M., Álvarez, P.M., Beltrán, F.J., 2015. Determination of main species involved in the first steps of TiO₂ photocatalytic degradation of organics with the use of scavengers: the case of ofloxacin. Appl. Catal. B 178, 44–53.

Rodríguez-Padrón, D., Luque, R., Muñoz-Batista, M.J., 2020. Waste-derived materials: opportunities in photocatalysis. Top. Curr. Chem. 378, 3.

Ruppert, G., Bauer, R., Heisler, G., 1993. The photo-Fenton reaction — an effective photochemical wastewater treatment process. J. Photochem. Photobiol. A Chem. 73, 75–78.

Seshachalam, U., Haribabu, B., Chandrasekhar, K.B., 2007. A novel validated LC method for quantitation of lopinavir in bulk drug and pharmaceutical formulation in the presence of its potential impurities and degradation products. Biomed. Chromatogr. 21, 716–723.

Sieber, K., Kourtakis, K., Kershaw, R., Dwight, K., Wold, A., 1982. Preparation and photoelectronic properties of FeWO₄. Mater. Res. Bull. 17, 721–725.

Thi, L.-A.P., Panchangam, S.C., Do, H.-T., Nguyen, V.-H., 2021. Prospects and challenges of photocatalysis for degradation and mineralization of antiviral drugs. In: Nguyen, V.-H., Vo, D.-V.N., Nanda, S. (Eds.), Nanostructured Photocatalysts: From Fundamental to Practical Applications. Elsevier, Amsterdam, pp. 489–517.

Tian, S.H., Tu, Y.T., Chen, D.S., Chen, X., Xiong, Y., 2011. Degradation of Acid Orange II at neutral pH using Fe₂(MoO₄)₃ as a heterogeneous Fenton-like catalyst. Chem. Eng. J. 169, 31–37.

Tiwari, R.N., Bonde, C.G., 2011. LC, LC-MS/TOF and MSn studies for the separation, identification and characterization of degradation products of ritonavir. Anal. Methods 3, 1674–1681.

Vargas, R., Madriz, L., Márquez, V., Torres, D., Kadirova, Z.C., Yubuta, K., Hojamberdiev, M., 2022. Elucidating the enhanced photoelectrochemical performance of ZnS/ZnO heterojunction and adsorption of water molecules by molecular dynamics simulations. Mater. Sci. Semicon. Process.

Wang, N., Zhang, J., Zhou, P., Zhang, Y., Li, W., Cheng, F., Pan, Z., Liu, Y., Lai, B., 2021. Iron molydate catalyzed activation of peroxymonosulfate for bisphenol AF degradation via synergetic non-radical and radical pathways. Sci. Total Environ. 797, 149151.

Wang, W.-L., Wu, Q.-Y., Wang, Z.-M., Hu, H.-Y., Negishi, N., Torimura, M., 2015. Photocatalytic degradation of the antiviral drug Tamiflu by UV-A/TiO₂: kinetics and mechanisms. Chemosphere 131, 41–47.

Wang, X., Ma, E., Shen, X., Guo, X., Zhang, M., Zhang, H., Liu, Y., Cai, F., Tao, S., Xing, B., 2014. Effect of model dissolved organic matter coating on sorption of phenanthrene by TiO$_2$ nanoparticles. Environ. Pollut. 194, 31–37.

Woche, M., Scheibe, N., von Tümpling, W., Schwidder, M., 2016. Degradation of the antiviral drug zanamivir in wastewater – the potential of a photocatalytic treatment process. Chem. Eng. J. 287, 674–679.

Wu, Z., Xue, Y., He, X., Li, Y., Yang, X., Wu, Z., Cravotto, G., 2020. Surfactants-assisted preparation of BiVO$_4$ with novel morphologies via microwave method and CdS decoration for enhanced photocatalytic properties. J. Hazard. Mater. 387, 122019.

Xue, Y., Chen, Z., Wu, Z., Tian, F., Yu, B., 2021. Hierarchical construction of a new Z-scheme Bi/BiVO$_4$-CdS heterojunction for enhanced visible-light photocatalytic degradation of tetracycline hydrochloride. Sep. Purif. Technol. 275, 119152.

Yoon, Y.S., Suzuki, K., Hayakawa, T., Hamakawa, S., Shishido, T., Takehira, K., 1999. Structures and catalytic properties of magnesium molybdate in the oxidative dehydrogenation of alkanes. Catal. Lett. 59, 165–172.

Zhang, Q., Celorrio, V., Bradley, K., Eisner, F., Cherns, D., Yan, W., Fermín, D., 2014. Density of deep trap states in oriented TiO$_2$ nanotubes arrays. J. Phys. Chem. C 118, 18207–18213.

Zhang, X., Ma, Y., Xi, L., Zhu, G., Li, X., Shi, D., Fan, J., 2019. Highly efficient photocatalytic removal of multiple refractory organic pollutants by BiVO$_4$/CH$_3$COO (BiO) heterostructured nanocomposite. Sci. Total Environ. 647, 245–254.

Zhang, Z., Hu, C., Hashim, M., Chen, P., Xiong, Y., Zhang, C., 2011. Synthesis and magnetic property of FeMoO$_4$ nanorods. Mater. Sci. Eng. B 176, 756–761.

Zwiener, C., Frimmel, F.H., 2000. Oxidative treatment of pharmaceuticals in water. Water Res. 34, 1881–1885.